NUCL SCI TECH (2020) 31:32
https://doi.org/10.1007/s41365-020-0741-9

Recent studies on potential accident-tolerant fuel-cladding systems in light water reactors

Sheng-Li Chen[1,2] · Xiu-Jie He[1] · Cen-Xi Yuan[1]

Received: 14 December 2019 / Revised: 22 January 2020 / Accepted: 22 January 2020 / Published online: 3 March 2020

Abstract Accident-tolerant fuel (ATF) has attracted considerable research attention since the 2011 Fukushima nuclear disaster. To improve the accident tolerance of the fuel-cladding systems in the current light-water reactors, it is proposed to develop and deploy (1) an enhanced Zr-based alloy or coated zircaloy for the fuel cladding, (2) alternative cladding materials with better accident tolerance, and (3) alternative fuels with enhanced accident tolerance and/or a higher U density. This review presents the features of the current UO_2–zircaloy system. Different techniques and characters to develop coating materials and enhanced Zr-based alloys are summarized. The features of several selected alternative fuels and cladding materials are reviewed and discussed. The neutronic evaluations of alternative fuel-cladding systems are analyzed. It is expected that one or more types of ATF-cladding systems discussed in the present review will be implemented in commercial reactors.

Keywords Accident-tolerant fuel · Accident-tolerant cladding · Light-water reactor · Neutronic evaluation

1 Introduction

Because it is reliable, stable, and environmentally sustainable, nuclear power is one of the most important forms of clean energy for reducing CO_2 emissions. Figure 1 shows the percentages of different sources of world electricity production in 2017 (25,721 TWh) [1]. Currently, nuclear power accounts for approximately 10% of the total world electricity production. Nuclear energy is one of the most important energy resources for development.

The current nuclear fuel is based on the UO_2–zircaloy system. The technology of the UO_2–zircaloy system is mature because of the development and operation experience gained over the past half-century. The operational record of the UO_2–zircaloy fuel rod was excellent under different conditions until the 2011 Fukushima Daiichi nuclear accident. The Fukushima accident indicated that the production of H_2 by the chemical reaction between Zr and water steam is drastic for the zircaloy cladding. It is widely recognized that the development of accident-tolerant fuel (ATF) is of great importance for increasing the accident tolerance for Gen-II and Gen-III light-water reactors (LWRs) under design-basis accident (DBA) and beyond-DBA (BDBA) conditions.

To improve the fuel performance under DBA and BDBA conditions, it is necessary to improve the accident tolerance of the fuel and cladding. The improvement of the

This work was supported by the National Key Research and Development Program of China (No. 2018YFB1900405), the National Natural Science Foundation of China (No. 11775316), the Tip-top Scientific and Technical Innovative Youth Talents of Guangdong Special Support Program (No. 2016TQ03N575), the Fundamental Research Funds for the Central Universities (No. 19lgpy299), the Science and Technology Planning Project of Guangdong Province, China (No. 2019A050510022), and the Nuclear Power Institute of China (No. HT-ATF-14-2018001).

✉ Xiu-Jie He
hexiujie@mail.sysu.edu.cn

✉ Cen-Xi Yuan
yuancx@mail.sysu.edu.cn

[1] Sino-French Institute of Nuclear Engineering and Technology, Sun Yat-sen University, Zhuhai 519082, China

[2] Université Grenoble Alpes, I-MEP2, 38402 Saint Martin d'Hères, France

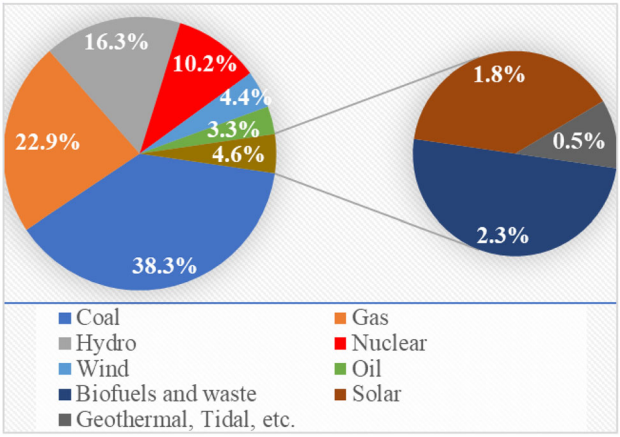

Fig. 1 (Color online) Sources of world electricity production in 2017 [1]

cladding mainly involves the reduction of oxidation, which generates H_2 and produces heat through chemical reactions. The following methods have been proposed [2].

(1) Using a Zr-based cladding with better oxidation resistance and mechanical strength, i.e., improve the Zr-based materials and coating-layer design.
(2) Using alternative cladding materials with a high oxidation resistance and strength.
(3) Using an alternative fuel with a high thermal conductivity and/or high U density.

The improved oxidation-resistant Zr-based alloy has similar neutronic characteristics to the current zircaloy and can be deployed in a relatively short time owing to the limited changes in the present design basis and the corresponding regulations. The highly oxidation-resistant coating can protect the zircaloy cladding from a chemical reaction with high-temperature water, which was the primary source of the H_2 explosion in the Fukushima accident. Alternative cladding materials provide diversity for the development of an accident-tolerant cladding. The two approaches for improving the performance of the cladding are similar. Approach (1) can be deployed in a relatively short time, while approach (2) can potentially provide more significant improvements. Notably, increasing the specific heats of both the fuel and the cladding is helpful for delaying the melting of the cladding under DBA and BDBA conditions.

Compared with the currently used ceramic UO_2 fuel, improved accident-tolerant alternative fuels have one or more additional features, e.g., improved fission production retention, a higher thermal conductivity, a higher specific heat capacity, and a higher U (or actinide) density. Alternative fuels provide diversity for developing an ATF. However, because their fuel performance differs significantly from that of the currently used UO_2 fuel, a relatively long time is needed to change the design basis and the corresponding regulations for deploying alternative fuels. Some nuclear fuels and cladding materials of Gen-IV or fusion reactors are considered and investigated as candidate accident-tolerant fuels and claddings.

The remainder of this paper is organized as follows. We introduce the characteristics of the currently used UO_2–zircaloy system in Sect. 2. Different technologies for approach (1) are reviewed in Sect. 3. In the light of the various possibilities for alternative cladding materials and alternative fuels, Sects. 4.1 and 4.2 briefly discuss the properties of some selected alternative fuels and claddings, respectively. Neutronic studies on ATF fuel-cladding systems are described in Sect. 5. Section 6 summarizes this review.

2 Current UO_2–Zr alloy system

UO_2 fuel is widely used in LWRs because of its high melting point, compatibility with water (coolant), and stability under irradiation [3]. The well-known disadvantage of UO_2 fuel is its low thermal conductivity, which results in a large temperature gradient from the surface to the center of the fuel pellet. Owing to the extensive use of UO_2 over the past decades, its properties have been widely studied. One of the most commonly used formulae for the thermal conductivity of UO_2, i.e., λ_{UO_2}, was proposed by Fink [4]:

$$\lambda_{UO_2}(t) = \left(7.5408 + 17.692t + 3.6142t^2\right)^{-1} + 6400t^{-2.5}\exp(-16.35/t), \quad (1)$$

where λ_{UO_2} has units of W/(K m), and $t = T/1000$ (with the temperature T given in K). This empirical formula is valid from room temperature to approximately the melting point of UO_2. The isotopic components of the fuel vary with burnup owing to a considerable number of nuclear reactions, particularly nuclear fission from U. The relationship between the burnup and the thermal conductivity of UO_2 is described in Ref. [5].

Notably, the isotopic components of nuclear fuel depend on not only the burnup but also the operating history. In the experimental data of Fig. 2 [4], discrepancies are observed among different measurements. Thus, all the semiempirical formulae for describing the thermophysical properties of UO_2 fuel are reasonable approaches, with certain deviations.

The design of dual-cooled annular fuel rod is considered to increase the safety margin for the melting of UO_2 fuel. Table 1 presents a comparison of the average and peak temperatures of UO_2 fuel with the typical cylindrical and dual-cooled annular designs [6, 7]. As shown, the annular

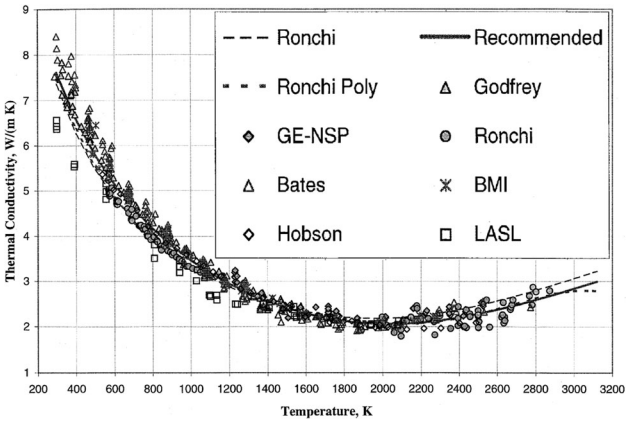

Fig. 2 Thermal conductivity of UO_2. The figure is from Ref. [4]

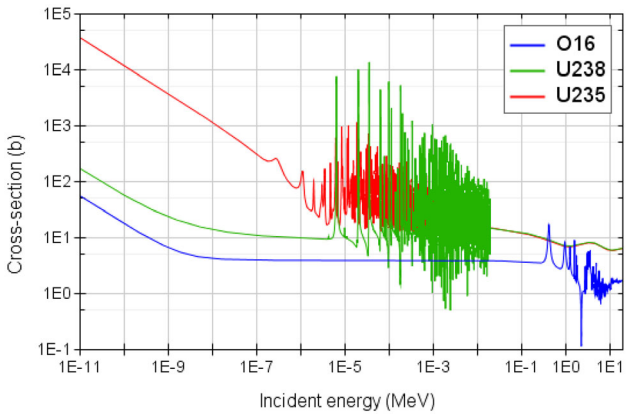

Fig. 3 (Color online) Total cross sections of ^{235}U, ^{238}U, and ^{16}O. The data are from the JEFF-3.1.1 nuclear data library [8]

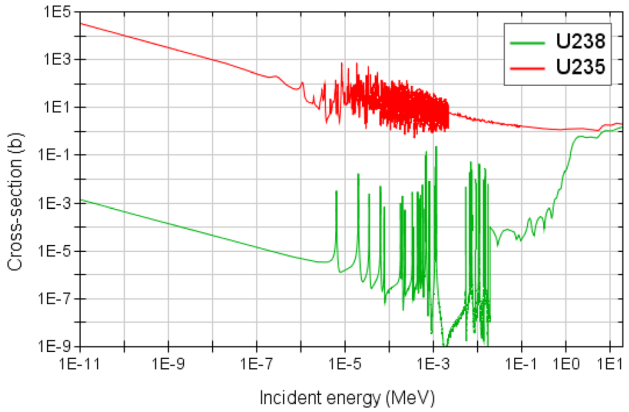

Fig. 4 (Color online) Fission cross sections of ^{235}U and ^{238}U. Data are from the JEFF-3.1.1 nuclear data library [8]

design can reduce the average and peak fuel temperatures by approximately 100 and 300 K, respectively.

From a neutronic view point, the use of uranium oxide UO_x can optimize the utilization of neutrons in the fuel pellet and increase the efficiency of the chain reaction in the reactor. Figure 3 illustrates the total neutron reaction cross sections of ^{235}U, ^{238}U, and ^{16}O according to data from the Joint Evaluated Fission and Fusion (JEFF)-3.1.1 nuclear data library [8]. The JEFF-3.1.1 data are presented herein because they well reproduce the measurements performed in a CEA integral benchmark experiment (PERLE) [9–13]. In nature, 99.8% of O isotopes are ^{16}O, which is a double-magic nucleus. Therefore, the neutron reactions with O in UO_x are generally negligible compared with the reactions with U.

In nature, 0.005%, 0.72%, and 99.274% of U isotopes are ^{234}U, ^{235}U, and ^{238}U, respectively. However, as indicated by the neutron fission cross sections in Fig. 4, the fission cross section of the major isotope ^{238}U is smaller than that of ^{235}U. Therefore, to increase the fission reaction rate in UO_2 fuel, the amount of the fissile isotope ^{235}U must be increased. The ^{235}U enrichment in current LWRs ranges from 3.5 to 5%. Because ^{235}U and ^{238}U have identical chemical properties, the separation of these two U isotopes should be based on their different masses.

As shown in Fig. 4, the fission cross section of ^{235}U in the thermal energy region is significantly higher than that in the fast energy region. Consequently, in the current design of LWRs, the fission neutrons are thermalized to increase the fission reaction rate. Figure 5 shows the typical neutron flux spectra for the current UO_2–Zr system at the beginning of life (BOL) and the end of life (EOL). The peaks of the thermal neutrons in the current LWRs design are optimized for the efficient use of neutrons for ^{235}U fission.

Zr-based materials are selected as the fuel-cladding materials because of the small neutron absorption cross section of Zr. Figure 6 shows the neutron-radiative capture cross sections of Zr isotopes in comparison with that of ^{56}Fe. Table 2 presents the total and radiative capture cross sections of Zr isotopes in comparison with those of ^{56}Fe at the thermal energy based on JEFF-3.1.1 [8], the latest European release JEFF-3.3 [15], and the latest American release ENDF/B-VIII.0 [16]. Figure 6 and Table 2 indicate that the neutron capture cross sections of Zr isotopes with even neutron numbers are > 10 times smaller than that of ^{56}Fe, which is the most abundant isotope in natural Fe. The

Table 1 Temperatures of cylindrical and annular UO_2 fuel [6, 7]

	Cylindrical UO_2 fuel	Annular UO_2 fuel
Average temperature (°C)	959	864
Peak temperature (°C)	1519	1226

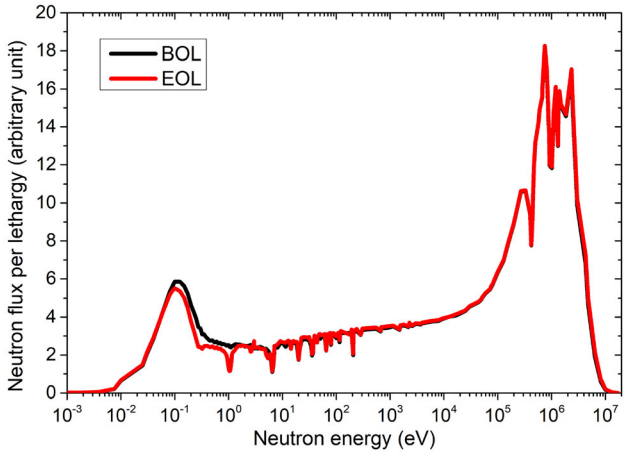

Fig. 5 (Color online) Neutron flux spectra for the current UO_2–Zr system at the BOL and EOL [14]

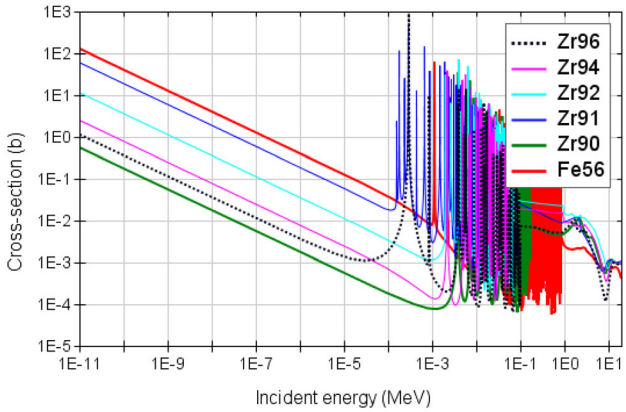

Fig. 6 (Color online) Radiative capture cross sections of Zr isotopes and ^{56}Fe. Data are from the JEFF-3.1.1 nuclear data library [8]

second-to-last column in Table 2 presents the cross sections of natural Zr, which is denoted as ^{nat}Zr. The cross sections of the natural Zr are only presented for comparison; the natural elements should not be used in the depletion calculation, because different isotopes have different cross sections.

Different Zr-based alloys have been developed in the past decades using different alloying elements to improve the performance, such as mechanical strength. Table 3 presents the components of different types of zircaloys. One of the most commonly used zircaloys in pressurized water reactors (PWRs) is zircaloy-4, which is hereinafter denoted as Zr-4. The thermal conductivity of Zr-4 is [17]

$$\lambda_{Zr-4}(T) = 11.3 + 2.25 \times 10^{-3}T + 7.25 \times 10^{-6}T^2. \quad (2)$$

The second-order coefficient in the original expression is $7.25 \times 10^{-7}T^2$ [17]. We changed the power from -7 to -6 according to the experimental data from Ref. [17]. Additionally, because the experimental measurements are taken from room temperature to approximately 1000 K, this expression is valid below 1000 K. The International Atomic Energy Agency (IAEA) recommended the following thermal conductivity of zircaloy according to experimental data for zircaloy-2 and Zr-4 [18]:

$$\lambda_{Zr-4}(T) = 11.3 + 2.25 \times 10^{-3}T + 7.25 \times 10^{-6}T^2. \quad (3)$$

This formula is valid, with an uncertainty of 4–7% for temperatures ranging from 300 K to approximately 1800 K.

Over the past approximately 60 years of development, zircaloy has been highly optimized through various experiments and industrial feedback. The critical problems with the mechanical behavior of UO_2–zircaloy were presented by Wang et al. [20]. A main drawback of zircaloy in LWRs is that Zr reacts with water steam at high temperatures:

$$Zr + H_2O \rightarrow ZrO_2 + 2H_2. \quad (4)$$

This reaction produces H_2, which increases the pressure in the reactor pressure vessel and the concrete containment. This was the primary source of H_2 exposure in the Fukushima Daiichi nuclear accident. Therefore, the idea of an ATF cladding is to add a coating to the zircaloy or replace the zircaloy with another cladding material to prevent or reduce the production of H_2 under accident conditions. The dynamic response of the Chinese CAP1000

Table 2 Thermal neutron total and radiative capture cross sections of Zr isotopes in comparison with ^{56}Fe

Isotope	^{90}Zr	^{91}Zr	^{92}Zr	^{94}Zr	^{96}Zr	^{Nat}Zr	^{56}Fe
Isotopic abundance (%)	51.45	11.22	17.15	17.38	2.80	100.00	–
Total cross section (barn)							
JEFF-3.1.1	5.41	11.84	7.38	6.23	6.19	6.63	14.79
JEFF-3.3	5.54	11.13	7.38	8.71	5.76	7.04	14.79
ENDF/B-VIII.0	5.31	10.95	7.29	8.71	4.87	6.86	14.80
Radiative capture cross section (barn)							
JEFF-3.1.1	0.011	1.202	0.229	0.050	0.023	0.189	2.58
JEFF-3.3	0.010	1.216	0.229	0.050	0.023	0.190	2.59
ENDF/B-VIII.0	0.010	1.205	0.226	0.050	0.020	0.189	2.61

Table 3 Compositions (in wt%) of main zircaloys other than Zr

Element[a]	Sn	Fe	Cr	Ni	Nb	O
Zr-2	1.2–1.7	0.07–0.2	0.05–0.15	0.03–0.08	–	~ 0.001
Zr-4	1.2–1.7	0.18–0.24	0.07–0.13	–	–	~ 0.001
Zr–1Nb[b]	–	–	–	–	1	~ 0.001
Zr–2.5Nb	–	–	–	–	2.5	~ 0.001

[a]Elements with a mass percentage of < 0.001%, such as Al, Hf, Si, C, and N, are not included in this table. Details for Zr-2 and Zr-4 can be found in Ref. [19]

[b]Zr–1Nb is known as M5®

containment under steam explosion accidents can be simulated in detail using the models developed by Sun Yat-sen University and the China Nuclear Power Technology Research Institute [21].

3 Surface-modified Zr-based cladding

Because the aforementioned approach (1) for the ATF cladding can be deployed in a relatively short time, extensive studies have been performed on it in the past several years. This section reviews different coating materials and improved Zr-based alloys. The coating materials are presented in the following order: metallic coatings, nonmetallic coatings, ceramic coatings, and oxide dispersion-strengthened (ODS) coatings. Ion-implanted improved zircaloys are briefly reviewed at the end of this section.

3.1 Metallic coatings

3.1.1 Pure Sn

Thin and uniform Sn coatings were deposited on Zr-4 by evaporation under vacuum conditions (10^{-5} Torr) [22]. Because the Sn coating was between the alloy and the oxide as a liquid agent, the oxidation performance of Zr-4 was improved. After oxidization in 250-Torr O_2 at 500 °C and corrosion in high-pressure water at 349 °C and 176 atm, the rates of both reactions of the Sn-coated Zr-4 decreased with the increasing thickness of the Sn coating.

3.1.2 Y coating

Y is widely investigated because of its oxidation resistance. It is expected to form stable, protective yttrium oxide at high temperatures, potentially reducing the oxidation of zircaloy-2. After exposure to supercritical water at 400 °C for 168 h, for untreated zircaloy-2, the formation of a fully developed zirconia layer and a subsurface O diffusion zone occurs. For Y-coated zircaloy-2 after oxidation at a high temperature, the surface-generated Y_2O_3 prevents the O from further diffusing into the interior [23].

3.1.3 Pure Cr

Cr is the most recognized ATF coating in the world because of its resistance to corrosion in the LWR coolant, its stability under neutron irradiation (260–400 °C), and its resistance to high-temperature steam oxidation [24]. AREVA in France fabricated a physical vapor deposition prototype machine to prepare a Cr coating on a full-length zircaloy cladding [25]. At present, the main countries in which pure Cr coatings are studied are France (AREVA/CEA/EDF), South Korea (KAERI), the USA (UIUC, University of Wisconsin-Madison, and University of Michigan), and China (Sun Yat-sen University).

The performance of the Cr-coated zircaloy was investigated at CEA in the framework of the French Nuclear Institute, in partnership with AREVA and EDF [26–28]. The results indicated that compared with the traditional uncoated zircaloy, the developed Cr coating significantly improved the high-temperature oxidation and mechanical properties (i.e., ductility and strength) of the zircaloy. In Park's study, an arc ion plating technique was used to coat a Cr layer onto the surface of Zr-4 as an anti-oxidation coating. The pure Cr phase was identified by X-ray diffraction (XRD) analysis, and the Cr film was compact and uniform. A Cr film on Zr-4 successfully acted as a corrosion-protective layer even in a 1473-K high-temperature steam environment [29]. In Korea, Kim et al. investigated the effects on coating structures and properties of different parameters, i.e., the laser beam power, inert gas flow, cooling of Zr-based alloys, and Cr powder control, in the deposition of a Cr coating by three-dimensional laser coating technology [30, 31]. After a high-temperature oxidation test, the Cr coating successfully acted as a corrosion barrier layer. Additionally, after both ring-compression and tensile tests, the Cr coating did not peel off, indicating that the adhesion property of the coating was excellent. Cr coatings were also prepared on a Zr-4 alloy by multi-arc ion plating by our research team [32], and the

effects of the bias and air pressure on the oxidation properties of the coatings were examined in detail. The results indicated that the bias potential and air pressure had significant effects on the oxidation performance and that the oxidation resistance of the Cr coating decreased when the bias pressure and air pressure were too high or low, as shown in Fig. 7. If the Cr coating is deposited directly on the surface of the Zr alloy, it causes mutual diffusion between the Zr and Cr. A large amount of Cr-rich precipitates can be observed in the Zr alloy substrate upon cooling [33].

In addition to the oxidation and mechanical properties, the irradiation effects were investigated in detail. Jiang et al. at the University of Michigan found that the irradiation effect of the Cr coating is related to not only the dose but also the coating thickness [34]. Owing to the smaller columnar grains and larger lattice distortion in thinner coatings, the evolution of the irradiation defects is delayed.

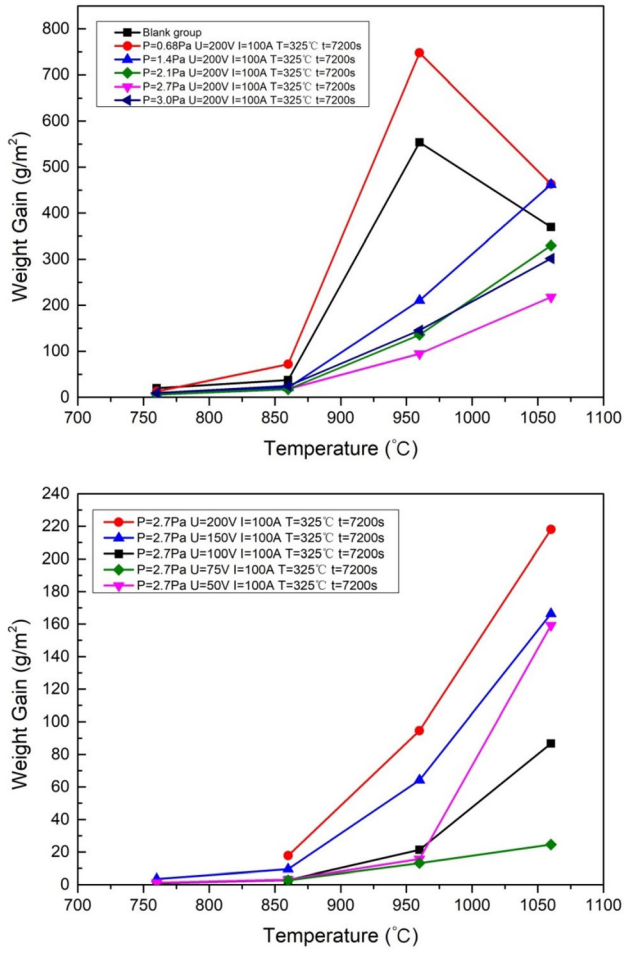

Fig. 7 (Color online) Weight gain of the Zr-4 alloy without and with a Cr coating deposited at different gas pressures (upper) and bias potentials (lower)

3.1.4 *Cr-based binary alloys*

At present, the main countries in which Cr-alloy coatings, e.g., CrAl coatings, are studied are South Korea (KAERI) and the USA (UIUC).

For the CrAl coating, the addition of Al can modify the structure of the coating and affect its oxidation performance [35]. When the Al content is high, the coating forms cubic γ-Al_2O_3 after high-temperature oxidation, and when the Al content is low, the coating produces Cr_2O_3 and Al_2O_3 simultaneously after high-temperature oxidation. The thickness of the CrAl coating deposited at KAERI in Korea ranged from 40 to 60 μm [36]. Because the CrAl binary alloy had higher strength than the Zr alloy, the mechanical properties of the modified surface, i.e., the creep and wear resistance, were improved.

3.1.5 *Fe-based alloys*

At present, the main countries in which Fe-based alloy coatings are studied are South Korea (KAERI) and the USA (UIUC).

For Fe-based alloys, such as FeCrAl, it is necessary to add a barrier layer at the coating/substrate interface to prevent the formation of Zr–Fe eutectic at high temperatures [7]. According to the UIUC research team, yttria-stabilized zirconia (YSZ) and zirconia have the potential to act as a barrier layer [37]. In contrast, the KAERI team selected a barrier layer of Cr [36] or Mo [38]. The thickness of an FeCrAl coating deposited at KAERI in Korea ranged from 40 to 60 μm [36]. An oxidation experiment indicated that the FeCrAl had good performance as a coating material on the ATF cladding. In addition to the formation of a eutectic with Zr, the significant neutronic penalty is a disadvantage of FeCrAl as an ATF cladding coating [39].

3.1.6 *High-entropy alloy*

Since the high-entropy alloy was proposed by Yeh of National Tsinghua University (Taiwan, China) in 2004 [40], it has rapidly attracted attention owing to its high strength/hardness, good oxidation resistance, outstanding wear resistance, and superior radiation resistance. Zhang et al. at Sichuan University, China, prepared a AlCrMoNbZr high-entropy alloy coating for ATF [41]. A corrosion experiment was performed over 1 month in an autoclave at 360 °C and 18.7 MPa. The results indicated that no zircaloy substrate oxides were formed, indicating the excellent corrosion resistance of the high-entropy alloy coating. Zhang et al. also prepared AlCrMoNbZr/(AlCrMoNbZr)N multilayer high-entropy alloy coatings used it for an ATF cladding [42]. Compared with the single-layer

AlCrMoNbZr or (AlCrMoNbZr)N coating, the AlCrMoNbZr/(AlCrMoNbZr)N multilayer coating can more effectively inhibit the diffusion of Al and the formation of the boehmite phase. A 50/50-nm AlCrMoNbZr/(AlCrMoNbZr)N multilayer coating exhibited higher corrosion resistance than 5/5-nm and 10/10-nm multilayer coatings.

3.2 Nonmetallic coatings

3.2.1 Pyrolytic C (PyC) coating

To mitigate the pellet cladding interaction–stress corrosion cracking problem and improve the accident tolerance, a PyC coating was deposited using a thermal cracking method on the inner surface of Zr-4 tubes [43, 44]. Although the authors did not perform high-temperature oxidation or corrosion experiments, they investigated factors affecting the coating process in detail, e.g., the temperature, time, and flow rate.

3.2.2 Polycrystalline diamond (PCD) coating

A PCD coating with a thickness of 300 nm was used to protect the nuclear fuel cladding of a Zr alloy from undesirable oxidation while preserving its function, without the loss of chemical stability [45]. Experimental results indicated that the PCD coating had good radiation resistance and high-temperature steam oxidation resistance. The experimental results of Ashcheulov et al. indicated that the weight gain of a Zr alloy protected by a PCD coating grown using a microwave plasma-enhanced linear antenna chemical vapor deposition apparatus was 47% lower than that of the Zr alloy without PCD protection after oxidation at 950 °C [46].

3.2.3 Si or silicide coating

Si coatings were applied to the surface of a Zr-based alloy by the plasma spray (PS) and laser beam scanning (LBS) methods [47]. In a high-temperature oxidation test at 1200 °C, there were problems with the PS coating technology, such as pore formation and interfacial oxidation caused by weak adhesion. To solve the problems of the PS coating method, LBS treatment was applied to the surface of the PS coating. The pure Si coating was transformed into a Si–Zr mixed layer, and the pores in the Si coating were successfully removed, as shown in Fig. 8. The interfacial oxidation was suppressed by the formation of diffusion bonds between the Zr-4 substrate and the Si–Zr mixed layer.

The air-oxidation behavior of Zr_2Si, ZrSi, and $ZrSi_2$ coatings deposited on a Zr alloy substrate by magnetron splashing at a low temperature was investigated [48]. The

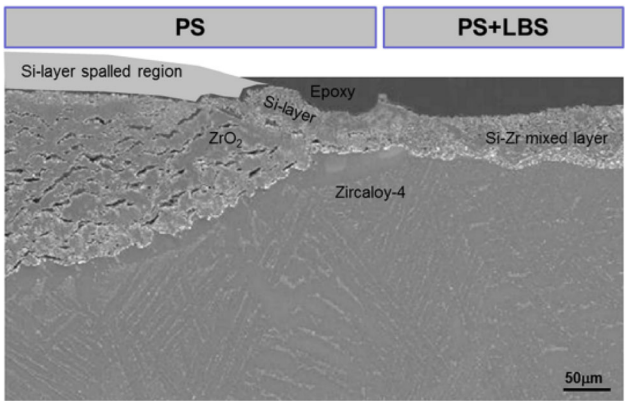

Fig. 8 Cross-sectional scanning electron microscopy image showing the microstructures obtained by PS and LBS treatment after PS coating following the high-temperature steam oxidation. The figure is from Ref. [47]

Ar pressure had a significant effect on the microstructure of the coating, and a lower pressure was beneficial for the formation of a denser and more protective microstructure. According to the oxidation results, $ZrSi_2$ was better than the other coatings, possibly owing to the formation of a protective layer composed of nanocrystalline SiO_2 and $ZrSiO_4$ in the amorphous Zr–Si–O matrix. A research group in the USA deposited a $ZrSi_2$ coating by magnetron sputtering, which exhibited excellent oxidation resistance [49]. After a severe thermal shock test, i.e., water quenching from 700 to 85 °C in 20 s, this coating exhibited no surface degradation, e.g., spallation or cracking.

3.3 Ceramic coatings

3.3.1 Nitrides

At present, the main countries in which nitride coatings are studied are Norway (IFE), the USA (Pennsylvania State University), and China (Sun Yat-sen University and the University of South China).

The research team at Pennsylvania State University, in conjunction with Westinghouse Electric Co., performed a detailed study on the corrosion of TiAlN and TiN coatings [50, 51]. They found that the TiAlN coating underwent Al depletion in a high-temperature water environment, yielding a boehmite phase. A layer of CrN was deposited on the outside of the TiAlN coating to solve this problem. Additionally, they studied alternating TiN and TiAlN layers and found that 8-layer TiN/TiAlN had the best corrosion resistance. A TiAlCrN coating was prepared by multi-arc ion plating by our research group [52]. Under corrosion at 18.5 MPa and 360 °C, the coating did not crack or fall off, and the weight gain of the coating was reduced by an order of magnitude compared with that of the original Zr alloy.

In Canada, Daub et al. from Canadian Nuclear Laboratories found that a CrN coating exhibited high corrosion resistance under PWR conditions, under CANDU conditions, and in a superheated steam environment [53]. Furthermore, they found that CrN and TiAlN coatings can reduce the H_2 ingress into Zr-4. Our research group deposited a CrN coating by multi-arc ion plating, and an oxidation experiment was performed from 760 to 1160 °C in an air environment [54]. Even after oxidation at 1160 °C, the coating remained intact and exhibited no sign of shedding or cracking. However, a typical feature of a nitride coating is that it decomposes at high temperatures. CrN and its decomposition products are also oxidized, and the possible chemical reactions involved are as follows:

$$2CrN \rightarrow Cr_2N + 1/2N_2 \quad (5)$$

$$Cr_2N \rightarrow 2Cr + 1/2N_2 \quad (6)$$

$$2CrN + 3/2O_2 \rightarrow Cr_2O_3 + N_2 \quad (7)$$

$$2Cr_2N + 3O_2 \rightarrow 2Cr_2O_3 + N_2 \quad (8)$$

$$4Cr + 3O_2 \rightarrow 2Cr_2O_3. \quad (9)$$

In the most recent study conducted by our group, although the CrN coating was excellent without damage after being oxidized at 1160 °C for 1 h, after two thermal cycles, i.e., 1160 °C → room temperature → 1160 °C → room temperature, the CrN coating began to fall off. This was due to the difference between the thermal expansion coefficients of the CrN ceramic coating and the Zr alloy. Therefore, our research group is currently studying the CrN gradient coating. As indicated by a mechanical analysis of a surface-coated zircaloy cladding, a spatial-gradient coating is more promising than a discrete coating [55]. Another research group in China performed a detailed analysis of the residual stress of a nitride coating deposited by magnetron sputtering [56]. The results indicated that the coating underwent compressive stress, and the residual stress of the coating prepared at a low sputtering power was higher than that for a high sputtering power. The results of another study confirmed that if the coefficient of thermal expansion of a TiN coating is significant, the coating peels off after the thermal shock resistance test [57].

Mandapaka et al. at the University of Michigan deposited two types of coatings (4-bilayer TiAlN/TiN and a TiN monolithic coating) on ZIRLO™ using cathodic arc physical vapor deposition [58]. The results of oxidation in supercritical water indicated that the zircaloy with the deposited coating was oxidized to a more degree than the original zircaloy, and a thick oxide layer was present between the coating and the substrate. This phenomenon was due to the penetration of the crack in the coating during the deposition process, which allowed O to contact the substrate through the coating.

3.3.2 $M_{n+1}AX_n$ (MAX) phases

At present, the main countries in which MAX phase coatings are studied are Germany (KIT), France (AREVA and CEA), and the USA.

In $M_{n+1}AX_n$ phases, M is an early transition metal, A is an A-group element (typically IIIA or IVA), and X is either C or N [59]. Owing to the good thermal stability of the MAX phase and the properties of both metals and ceramics, these materials have attracted increasing attention in recent years. Additionally, some phases, such as Ti_2AlC, are stable under neutron-irradiation conditions and are therefore promising for high-temperature nuclear applications [60]. Maier et al. deposited a Ti_2AlC coating on the surface of Zr-4 by the cold spray technique and performed oxidation experiments in an air environment at 700 °C and in water vapor at 1005 °C [61]. The oxidation resistance of the Zr alloy with the coating was significantly better than that of the Zr alloy without the coating. Although the MAX phase has many advantages, its preparation is challenging, mainly because this ternary system is likely to form compounds with other atomic ratios. For example, Yeom's Ti–Al–C coating obtained by magnetron sputtering was amorphous. However, a crystal structure of Ti_2AlC can be obtained by keeping the coating temperature at 900 °C for 3 s in laser surface treatment [62]. In research performed for a Master's thesis at the University of Tennessee, in situ high-temperature grazing incidence XRD results indicated that a Cr_2AlC MAX phase was formed when the temperature was increased to 500 °C [63].

The oxidation and mechanical properties of the ceramic coating are good. However, the fuel cladding can undergo diametrical compression when the reactor is in service. Ensuring that the brittle ceramic coating does not crack or fall off is a challenging problem [2]. To verify the feasibility of the Ti_3AlC_2 coating, Au ion irradiation and nanoindentation were performed to simulate the severe displacement damage and high pressure, respectively, applied to the cladding surface [64]. Even after irradiation to approximately 14 displacements per atom (DPA), no amorphization was observed in the coating. In a nanoindentation test, under a stress of 16.6 GPa, the coating was still not cracked. Another problem is that the A-group element, such as Al or Si, may diffuse out of the MAX phases and form intermetallics with the zircaloy [65]. For example, the amount of Al penetration into the zircaloy is roughly an order of magnitude larger than that of Si penetration. A research group at CEA in France verified that amorphous Cr–Al–C can be converted into Cr_2AlC by annealing the as-deposited coatings at a temperature below

that corresponding to the metallurgical degradation of the zircaloy [66].

3.3.3 SiC coating

In the field of ATFs, SiC is generally used to completely replace the Zr alloy in the body material. However, a research group in China deposited an SiC coating on Zr-4 by magnetron sputtering [67]. The results indicated that the dense SiC coating had excellent mechanical properties, with high hardness (25.61 GPa), elastic modulus (214.9 GPa), and critical load (8.24 N) values. In the future, it is necessary to study the oxidation performance of the SiC coating in detail.

3.4 ODS layer

The ODS layer differs from the two aforementioned coatings. Under LBS, it does not remain on the surface of the Zr alloy but permeates into the Zr alloy. The surface modification of the Zr alloy by LBS can improve the properties of the Zr alloy, e.g., increasing the wear resistance, increasing the corrosion resistance, and improving the strength. A schematic of the ODS treatment is shown in Fig. 9. Kim et al. in Korea used the LBS method to inject 10-μm Y_2O_3 particles into a 2-mm-thick Zr alloy to form an ODS structure [68, 69]. Y_2O_3 particles were uniformly distributed in an ODS-alloyed layer using LBS technology, without voids or cracks. The average particle size of the dispersed particles in the ODS layer was 20 nm, and the thickness of the ODS layer was 0.4 mm, accounting for 20% of the total thickness of the Zr-4 alloy sheet. At 500 °C, the yield strength of the Zr alloy covered with the ODS layer was $> 65\%$ higher than that of the initial Zr alloy. The increase in the strength was caused by the martensitic transformation of the Zr-4 alloy. Additionally, other coatings, such as Cr, Cr alloys, and FeCrAl/Cr, can be deposited on the ODS layer. The function of the ODS layer is to increase the high-temperature strength, and that of the surface coating is to increase the corrosion/oxidation resistance [70].

3.5 Modification by ion implantation

In 1987, ion-implantation experiments revealed the following: (1) The concentration and depth of the implanted ions can be effectively controlled, (2) ion implantation can improve the microhardness and wear properties of materials, and (3) ion implantation can significantly extend the lifetime of manufacturing tools in practical industrial applications [71]. Oxidation of zircaloy-2 in the nonsurface-treated condition and after ion implantation with N and C was conducted after exposure to an environment of pressurized water at 25 MPa and a temperature of 300 °C [23]. N and C ion implantation resulted in a thinner oxidation layer compared with the pristine zircaloy-2. To investigate the effect of Al addition on the air-oxidation behavior of a zircaloy, Peng et al. performed a series of irradiation tests on a ZIRLO alloy with different doses of Al ions [72]. The effect of the Al injection on the weight gain of the ZIRLO alloy is shown in Fig. 10. The oxidation weight gain of the ZIRLO alloy increased with the oxidation time in all cases, and the oxidation weight gain rate decreased with an increase in the irradiation dose. When the irradiation dose of Al reached 10^{18} ions/cm^2, the oxidation weight gain of the ZIRLO alloy was only 30% of that of the original sample, indicating that the oxidation properties of the Zr alloy can be significantly improved by irradiation with Al ions.

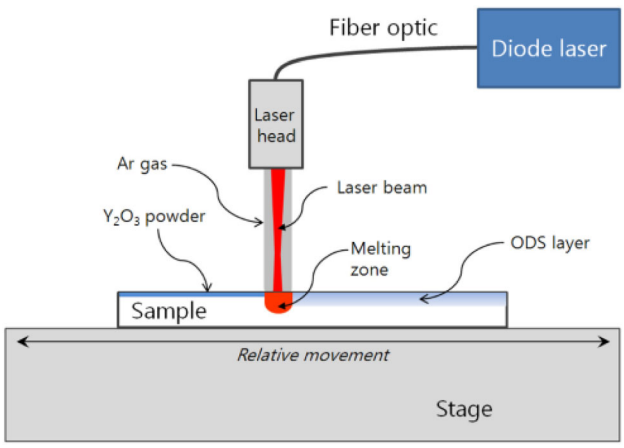

Fig. 9 Schematic of the ODS treatment. The figure is from Refs. [68, 69]

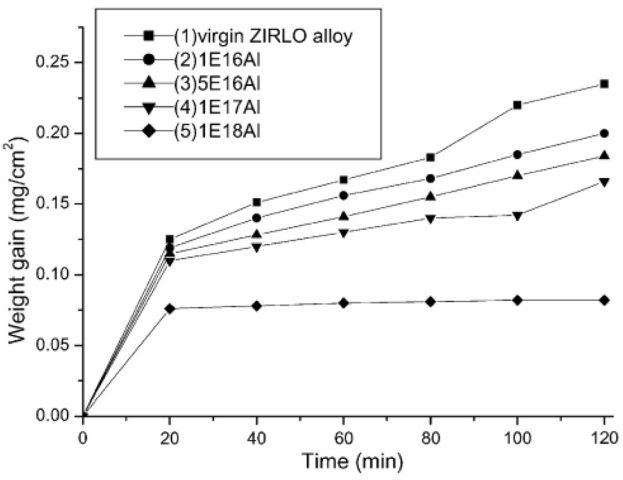

Fig. 10 Oxidation curves of the ZIRLO alloy implanted with Al at different fluences at 500 °C in air. The figure is from Ref. [72]

4 Alternative fuel-cladding system

The various alternative fuels and cladding materials and their combinations provide diversity for obtaining commercial nuclear fuel with a high efficiency and safety level. In the past years, many alternative materials have been proposed and considered for the ATF and cladding, and they are briefly reviewed in this section.

4.1 Alternative fuels

As mentioned in Sect. 2, UO_2 fuel has a low thermal conductivity. Therefore, alternative fuels with a higher thermal conductivity have been considered. There are two strategies to enhance the thermal conductivity of the nuclear fuel: (1) incorporating metal or other materials into the UO_2 fuel and (2) completely replacing the UO_2 fuel.

The former strategy is based on the current UO_2 fuel and thus can be deployed in the short term. However, incorporating metal into ceramic UO_2 fuel may reduce the melting point, as indicated by the examples in Table 4. Therefore, the margin for fuel melting must be quantified for regulatory reasons. Incorporating other components into UO_2 fuel reduces the U density in the fuel. One should increase the ^{235}U content (or introduce fissile Pu isotopes having larger thermal neutron fission cross sections than ^{235}U [73]) into the fuel or reduce the amount of absorber materials to maintain the reactivity for operation and the cycle length.

The latter strategy requires more time for development and deployment but can significantly improve the fuel performance. It is possible to obtain a fuel with both a higher thermal conductivity and a higher U density than UO_2 fuel, such as U_3Si_2 and UN fuels, which are discussed in the following subsections. Table 4 presents the percentages of U (and other included actinides in some cases) for different fuels.

4.1.1 UO_2–BeO

The loading of BeO in the UO_2 ceramic fuel can significantly improve the thermal conductivity of the fuel because BeO has a higher thermal conductivity than the ceramic UO_2 material. As indicated by the experimental data for the thermal conductivity of BeO presented in Ref. [78] and their interpretation by Zhou [79], the thermal conductivity of BeO is 22 times higher than that of UO_2 at room temperature. At 1500 K, the ratio of the thermal conductivity of BeO to that of UO_2 is 3 and 7 according to the Fink model [4] and the Harding and Martin (HM) formula [80], respectively.

Figure 11 presents the thermal conductivity for UO_2–BeO fuel with different volume fractions of BeO [81], in comparison with that of UO_2 fuel [4]. As shown, doping with BeO can significantly increase the thermal conductivity of the UO_2 fuel; 2.1% volumetric (= 0.6% by mass) loading of BeO can increase the thermal conductivity of UO_2 fuel by approximately 50% at 1800 K (and by > 50% if the HM model [80] is used for UO_2). According to Ref. [82], the thermal conductivity of UO_2–(4.2 vol%)BeO fuel at 1100 K is higher than that of UO_2 fuel by 10% or 25%, depending on the incorporation method. Additionally, the thermal conductivity of UO_2–BeO fuel was investigated by Li et al. using statistical continuum mechanics for BeO fractions ranging from 0 to 100% [83]. The thermal conductivity of UO_2–BeO fuel versus the volumetric content of BeO at room temperature computed using the statistical continuum model is shown in [83].

Many studies have been performed on UO_2–BeO fuels with different volume fractions of BeO. The irradiation behavior of 12% ^{235}U-enriched UO_2–(30 vol%)BeO fuel was tested by Johnson and Mills in 1963 [84]. Ishimoto et al. performed an experiment in which the thermal conductivity of UO_2 fuel was significantly improved by adding 1.1, 2.1, 3.2, 4.2, and 36.4 vol% BeO [82]. Chandramouli and Revankar developed a thermal model of UO_2–BeO fuel, which is used for analyzing the performance during a

Table 4 Proportions of actinides and melting points for different U-based fuels

Material	Weight percentage of actinides (%)	Melting temperature (°C)
UO_2	88.1	2847 [74]
U–10Zr	79.3	1350 [75]
U–10Mo	79.3	1150 [75]
U–19Pu–10Zr	79.3	1150 [76]
U–19Pu–10Mo	79.3	1000 [76]
U_3Si	96.2	
U_3Si_2	92.7	1665 [74]
UN	94.4 (94.1 for ^{15}N)	2630 [77]
UN–U_3Si_5	(83.6, 94.4)	
UN–U_3Si_2	(92.7, 94.4)	

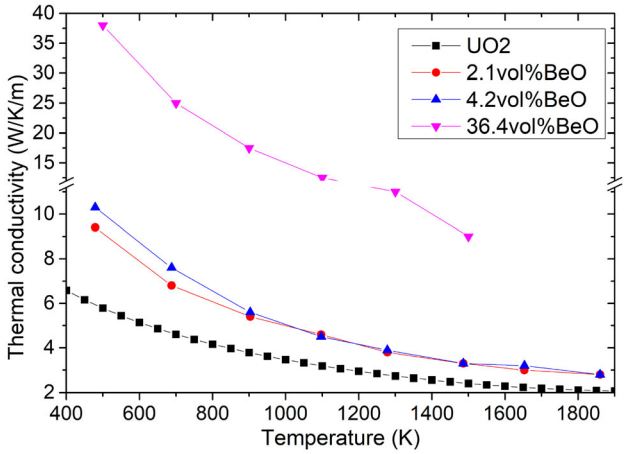

Fig. 11 (Color online) Thermal conductivity of UO_2 fuel incorporated with different volume fractions of BeO [81]

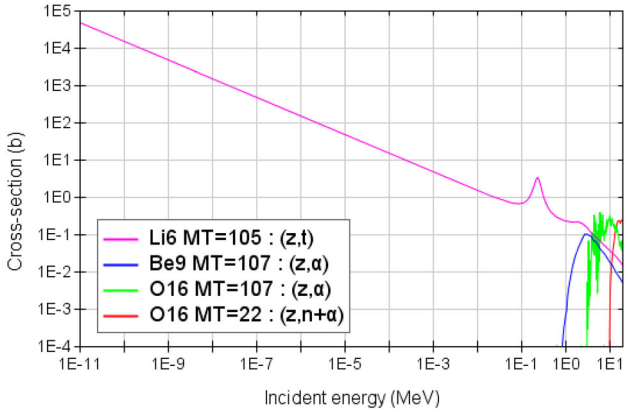

Fig. 12 (Color online) Gas production cross section of ^{9}Be (and the subsequent product ^{6}Li) and ^{16}O. The data are from the JEFF-3.1.1 nuclear data library [8]

loss-of-coolant accident (LOCA) [85]. The neutronic properties of UO_2–(5 vol%)BeO and UO_2–(10 vol%)BeO fuels were examined by Smith [86]. McCoy and Mays reported that the incorporation of BeO (4 and 9.6 vol%) can reduce the internal rod pressures and the fission gas release [87]. Recently, Zhou and Zhou studied the thermophysical and mechanical properties of UO_2–(36.4 vol%)BeO fuel with different claddings [79].

The doping of BeO requires an increase in ^{235}U enrichment for maintaining the cycle length. Because the cost of BeO is approximately five times higher than that of UO_2 fuel [88], the fabrication of UO_2–BeO fuel is more expensive than that of the current UO_2 fuel. However, it is possible to compensate for the additional cost of the fuel fabrication by extending the fuel cycle length.

Table 5 presents a comparison of the behavior of UO_2–Zr-4 and UO_2–(10 vol%)BeO–Zr-4 fuel-cladding systems under the LOCA condition [7]. As shown, the BeO-doped fuel can reduce the maximum plenum pressure and maximum fuel and cladding temperature and delay the rod failure under the LOCA condition.

An essential feature of ^{9}Be, which accounts for 100% of natural Be, is the relatively large (n, α) cross sections at a neutron energy of < 3 MeV, as shown in Fig. 12. Additionally, the product of the ^{9}Be (n, α) reaction is ^{6}He, which decays to ^{6}Li with a half-life of 0.82 s. As shown in Fig. 12, the (n, t) cross section of ^{6}Li is large, while both the tritium and ^{4}He from the ^{6}Li (n, t) reaction are in gaseous states. The small (n, α) cross sections of fissile and fissionable heavy nuclei have been evaluated in recently released nuclear libraries, such as ENDF/B-VIII.0 [16] and JEFF-3.3 [15]. Regardless of the fission products, the primary production of the He gas should come from ^{9}Be. The gas released from the fuel pellet increases the pressure in the gap between the fuel rod and the cladding. This results in the swelling of the fuel rod and an increase in the pin pressure.

4.1.2 U–Mo

Similar to the incorporation with BeO, Mo is incorporated into the current UO_2 fuel for increasing the thermal conductivity of the fuel and the subsequent margin for fuel melting. Figure 13 [89] presents the thermal conductivity of U–10Mo at different burnup levels with respect to the temperature (left) and at different temperatures with respect to the burnup level (right). It is noteworthy that the burnup (denoted as BU in Fig. 13) used in Ref. [89] is the relative consummation of ^{235}U by nuclear reactions other than radiative capture:

$$\mathrm{BU} = \frac{^{235}\mathrm{U}_0 - \left[^{235}\mathrm{U} + \left(^{236}\mathrm{U} - ^{236}\mathrm{U}_0\right)\right]}{^{235}\mathrm{U}_0}, \quad (10)$$

where the index 0 corresponds to the initial concentrations. The thermal conductivity is significantly increased by doping 10 wt% Mo (compared with data shown in Fig. 2).

Table 5 Comparison between UO_2–Zr-4 and UO_2–(10 vol%)BeO–Zr-4 fuel-cladding systems under LOCA conditions [7]

Fuel-cladding system	UO_2–Zr-4	(UO_2–10 vol% BeO)–Zr-4
Maximum plenum pressure (MPa)	5.08	4.95
Maximum fuel temperature (K)	1265.2	1196.0
Maximum cladding temperature (K)	1140.7	1091.3
Rod failure time (s)	61	68

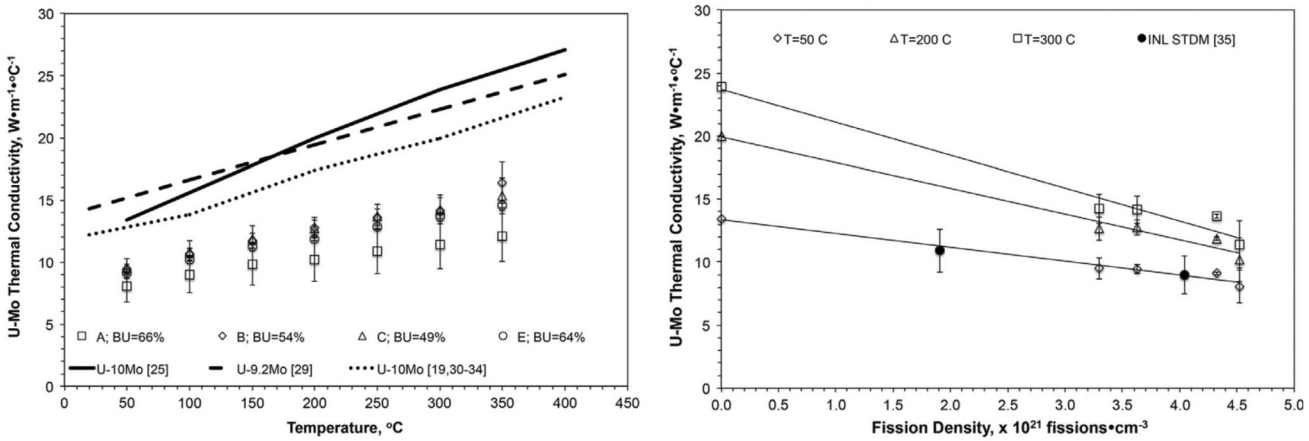

Fig. 13 Thermal conductivity of U–10Mo versus the temperature (left) and neutron fluence (right). The figures are from Ref. [89]

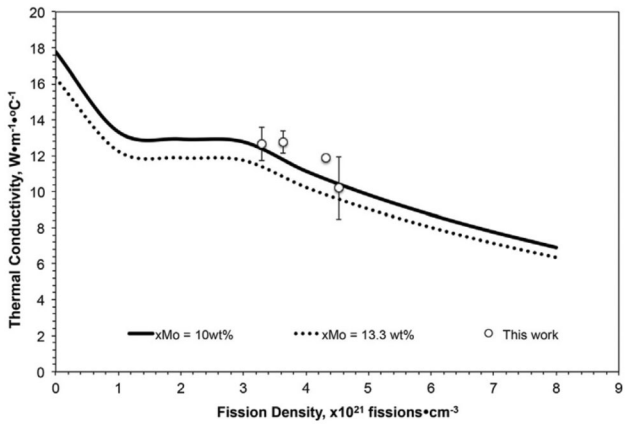

Fig. 14 Model-based thermal conductivity of U–10Mo and U–13Mo versus the temperature and neutron fluence at 200 °C. The points represent experimental measurements of U–10Mo performed by Burkes et al. [89]. The figure is from Ref. [89]

Figure 13 presents experimental measurements performed under different conditions. Figure 14 shows a plot of the model-based thermal conductivity of U–Mo [89]. The decreasing tendency of the thermal conductivity with the increasing burnup in Fig. 14 agrees with the data shown in Fig. 13. Additionally, Fig. 14 shows a counterintuitive tendency for the incorporation of different amounts of Mo: The 13.3 wt% Mo-doped fuel has slightly lower thermal conductivity than the 10 wt% Mo-doped fuel.

Notably, Mo can participate in a chemical reaction with water above 1000 °C [90]:

$$\mathrm{Mo} + 3\mathrm{H_2O} \rightarrow \mathrm{MoO_3} + 3\mathrm{H_2}. \quad (11)$$

H_2 is a primary source of reactor containment explosion accidents, such as the Fukushima accident. Even if the cladding encloses the Mo in the fuel under normal conditions, the process of H_2 production under accident conditions should be considered.

According to the neutron economy, Mo doping requires more ^{235}U in the fuel (greater enrichment or higher density) to achieve the same cycle length as the current fuel. Among the different Mo isotopes, ^{95}Mo has the largest neutron capture cross section in the thermal region. Table 6 presents the corresponding thermal neutron capture cross sections of JEFF-3.1.1 [8] and the isotopic abundance-weighted value. It can be concluded that ^{95}Mo contributes 85% of the thermal neutron capture reaction among all the isotopes that occur in nature. Therefore, a reduction of the ^{95}Mo content in the Mo material can significantly enhance the neutron economy of U–Mo fuel. For industrial applications, the optimization of Mo for incorporation into UO_2 fuel should consider the trade-off between the cost of reducing the content of ^{95}Mo and the enhancement in the neutron economy.

4.1.3 U_3Si_2

The U-Si binary is considered for ATF because of its thermodynamic stability [91]. Among the different U-Si binaries, U_3Si has the largest proportion of U. However, experiments indicated that the U_3Si fuel swells

Table 6 Thermal neutron-radiative capture cross sections (unit: barn) of Mo isotopes of JEFF-3.1.1 [8]

Isotope	^{92}Mo	^{94}Mo	^{95}Mo	^{96}Mo	^{97}Mo	^{98}Mo	^{100}Mo	Sum
Abundance (%)	14.65	9.19	15.87	16.67	9.58	24.29	9.74	99.99
Cross section	0.0208	0.0131	13.558	0.5951	2.0988	0.1299	0.1989	–
Average cross section	0.0030	0.0012	2.1517	0.0992	0.2011	0.0316	0.0194	2.5071

considerably under irradiation [92–94]. Moreover, it is dissociated into solid U and U_3Si_2 above 900 °C [74]. Among the U-Si binaries USi_2, U_3Si_5, USi, U_3Si_2, and U_3Si, U_3Si_2 has the second-highest U content (after U_3Si). Additionally, U_3Si_2 fuel has good performance under irradiation [92, 94] and several advantageous properties compared with UO_2 fuel [74]. Furthermore, tests involving burnup of up to 20 MWd/kgU indicated that U_3Si_2 fuel swells less than UO_2 and U_3Si_2 has less fission gas release than UO_2 [7].

Compared with the UO_2 fuel, the U_3Si_2 fuel has a significantly higher thermal conductivity. A semiempirical formula for conservatively describing the thermal conductivity of U_3Si_2 fuel is given as follows [95]:

$$\lambda_{U_3Si_2}(T) = 7.98 + 0.0051 \times (T - 273.15), \quad (12)$$

where T represents the temperature (in K). According to Ref. [95], this empirical formula is valid from room temperature to 1473 K. However, Shimizu reported that this linear expression corresponded to experimental data measured from 470 to 1150 K and overestimated the thermal conductivity below 200 °C [96]. Figure 15 shows the thermal conductivities of UO_2 [4] and U_3Si_2 [95] for temperatures ranging from 470 to 1150 K. The thermal conductivity of U_3Si_2 is higher than that of UO_2. With the increasing temperature, the thermal conductivity of U_3Si_2 increases, whereas that of UO_2 decreases. The increase in the thermal conductivity may be considered as an inherent safety characteristic of the U_3Si_2 fuel for releasing heat from the fuel. Moreover, the higher thermal conductivity allows more accident-tolerant claddings whose thermal performance is not as good as that of a zircaloy, such as SiC.

A drawback of the U-Si binary is its low oxidation resistance. As shown in Fig. 16 [91], the U_3Si_2 and U_3Si_5 fuels begin oxidizing at 270 °C, whereas the oxidation of the current UO_2 fuel begins at 390 °C. Additionally, for the U_3Si_2 fuel, the oxidation rate quickly increases with the temperature compared with U_3Si_5.

4.1.4 UN

Among the alternative fuel candidates, UN fuel has the highest U content. The thermal conductivity of UN fuel can be empirically calculated as follows [97]:

$$\lambda_{UN}(T) = 1.23T^{0.41}, \quad (13)$$

where T represents the temperature (in K), and λ_{UN} has units of W/(K m). This empirical formula is valid for temperatures below approximately 2000 K. The thermal conductivity of UN fuel based on this analytical formula is plotted as a function of the temperature in Fig. 15 in comparison with that of UO_2 fuel. Similar to the U_3Si_2 fuel, the thermal conductivity of the UN fuel increases with the temperature. As explained for the U_3Si_2 fuel, this may be considered as an inherent safety feature of the UN fuel. Additionally, the thermal conductivity of the UN fuel is significantly higher than that of the UO_2 fuel, while its melting point (2630 °C) [77] is comparable to that of the UO_2 fuel (2847 °C) [74]. Consequently, the use of UN fuel as an ATF can significantly increase the margin for fuel melting and allow the use of advanced claddings. Other physical properties, such as the lattice parameter, density, and thermal expansion coefficient, were correlated with the temperature by Hayes [98]. It is also noteworthy that the discrepancy of the experimental measurements for the thermal conductivity of the UN fuel (shown in Fig. 17 [99]) is greater than that in Fig. 2 for the UO_2 fuel.

The neutronic drawback of $U^{nat}N$ is a large reactivity penalty due to ^{14}N, which accounts for 99.6% of natural N. As shown in Fig. 18, the cross section of ^{15}N is smaller than that of ^{14}N below 0.1 MeV owing to the even neutron

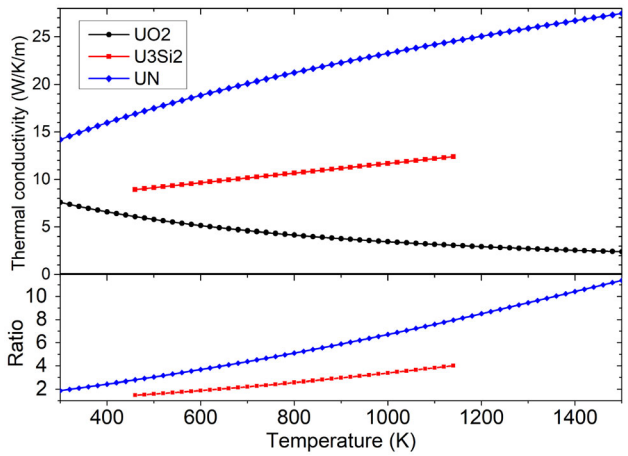

Fig. 15 (Color online) Thermal conductivities of UO_2 [4], U_3Si_2 [95], and UN [97]

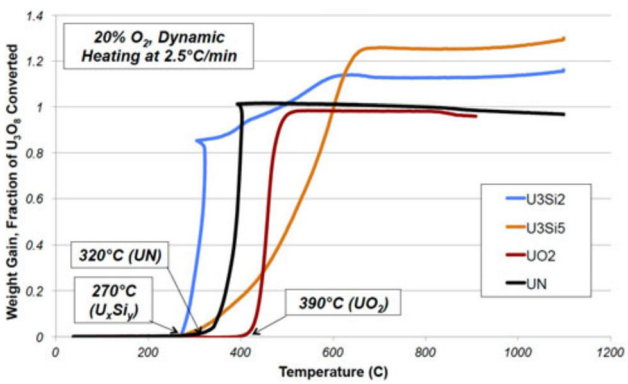

Fig. 16 (Color online) Oxidation results for U–Si with UO_2 and UN with respect to the temperature. The figure is from Ref. [91]

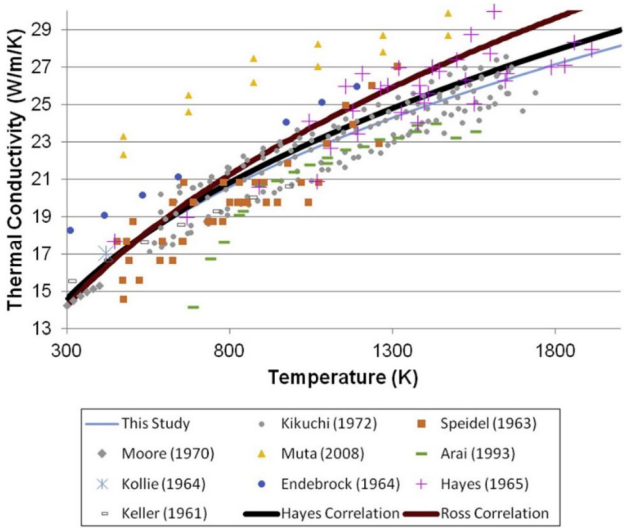

Fig. 17 (Color online) Thermal conductivity of the UN fuel. The figure is from Ref. [99]

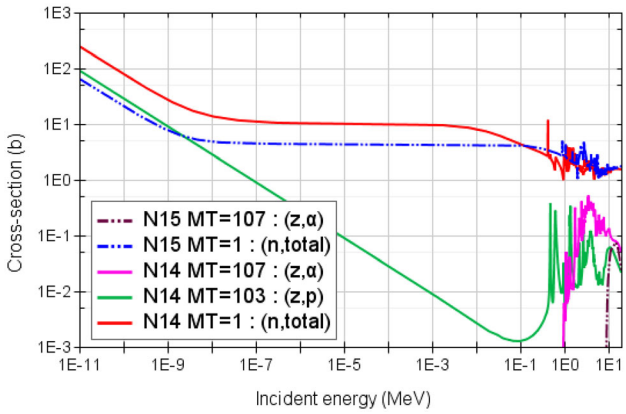

Fig. 18 (Color online) Cross sections of ^{14}N and ^{15}N. The data are from the JEFF-3.1.1 nuclear data library [8]

number of ^{15}N. Therefore, $U^{15}N$ was considered as a potential ATF [93]. The use of ^{15}N rather than natural N can prevent the production of long-life radiotoxic ^{14}C by the (n, p) reaction of ^{14}N, whose cross section is also shown in Fig. 18. Moreover, as shown in Fig. 18, the (n, α) cross section of ^{15}N is significantly smaller than that of ^{14}N. This indicates that replacing natural N with ^{15}N can reduce the production of He gas, which accelerates the fuel swelling and increases the pin pressure. Remarkably, the nuclear reactions of ^{14}N account for approximately 16% of the gas release (He and H_2) [7].

The enrichment of ^{15}N can significantly increase the performance of UN fuel. However, the cost of enrichment must be considered for deployment and industrial applications. At present, the most competitive enrichment processes cost approximately 30 Euros (approximately 235 yuan) per gram of ^{15}N [7]. As the cost of the fabrication of the current UO_2 fuel is approximately a few tens of yuan per gram, the cost of ^{15}N enrichment is an essential issue for $U^{15}N$ fuel. One possible method for reducing the cost of ^{15}N enrichment is the recycling of ^{15}N.

Another well-known disadvantage associated with UN fuel is its chemical reaction with water [100]. Above 250 °C, the following two reactions have been observed [7].

$$2UN + 4H_2O \rightarrow 2UO_2 + 2NH_3 + H_2 \quad (14)$$

$$3UN + 2H_2O \rightarrow UO_2 + U_2N_3 + 2H_2 \quad (15)$$

The production of H_2 through these reactions can potentially cause a H explosion. Lopes et al. reported that minimizing the open porosity can improve the water resistance of nitride fuel [101]. To avoid the chemical reaction with water, researchers have proposed the addition of other fuels that insulate the UN fuel from the water in the case of cladding failure, including UN–UO_2 [102], UN–U_3Si_5 [93], and UN–U_3Si_2 fuels [103]. In our previous publication [14], we proposed that the fully ceramic microencapsulated (FCM) fuel design [104–106] may be another possible solution for avoiding the chemical reaction between the UN fuel and water.

In addition to the chemical reaction with water, irradiation-induced swelling is an issue associated with UN fuel. Figure 19 presents the irradiation-induced volumetric swelling for different fuels [99]. As shown, the volumetric swelling of the UN fuel is > 3 times greater than that of the current UO_2 fuel and > 2 times greater than that of the U_3Si_2 fuel. Doping of the U_3Si_2 and UO_2 fuels can reduce the irradiation swelling of the UN fuel, but swelling is still a significant challenge for UN-based fuels.

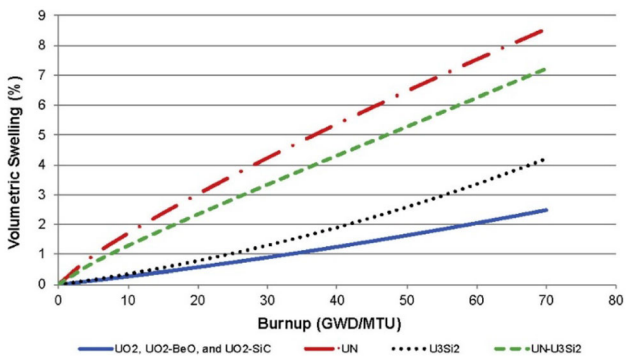

Fig. 19 (Color online) Volumetric swelling of different fuels under irradiation. Here, the UN–U_3Si_2 fuel contained 30% U_3Si_2. The figure is from Ref. [99]

4.2 Alternative claddings

To improve the accident tolerance of the nuclear fuel-cladding system, the use of alternative fuels and/or enhanced claddings is proposed. Two types of ATF claddings can be selected: a Zr-coated cladding or an alternative cladding. Zr-based claddings are discussed in Sect. 3. This subsection mainly focuses on the alternative claddings FeCrAl and SiC.

4.2.1 FeCrAl

Stainless steel (SS) has historically been used in LWRs [107–109]. Figure 20 shows the worldwide fuel failure rates from 1960 to 2010 [110]. Compared with a zircaloy cladding, an SS cladding leads to a higher likelihood of fuel failure in boiling water reactors (BWRs) but less failure in PWRs. Therefore, enhanced SSs are proposed as candidate materials for the ATF cladding. Among the different types of SSs, FeCrAl is considered as a candidate material for the ATF cladding. The addition of Cr and Al to SS can improve the oxidation resistance [111, 112]. Furthermore, the addition of Cr and Al can improve the neutron economy in LWRs owing to their smaller neutron capture cross sections compared with Fe (see Fig. 21). FeCrAl has better resistance to environmentally assisted cracking than modern-type 304SS [113]. Additionally, as indicated by the oxidation kinetics shown in Fig. 22 [114], the oxidation rate of FeCrAl is more than two orders of magnitude lower than that of a zircaloy [110]. The irradiation-induced atomic displacement damage was recently investigated [115]. The FeCrAl cladding material is currently being tested in commercial nuclear reactors [116].

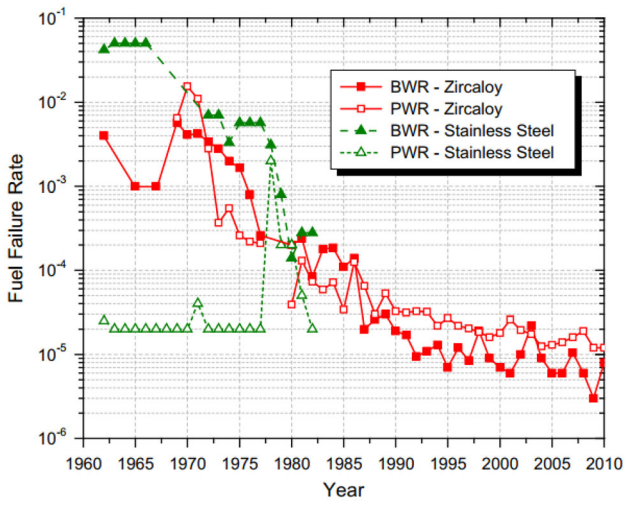

Fig. 20 (Color online) Worldwide historical fuel failure rates up to 2010 for zircaloy and SS claddings in LWRs. The figure is from Ref. [110]

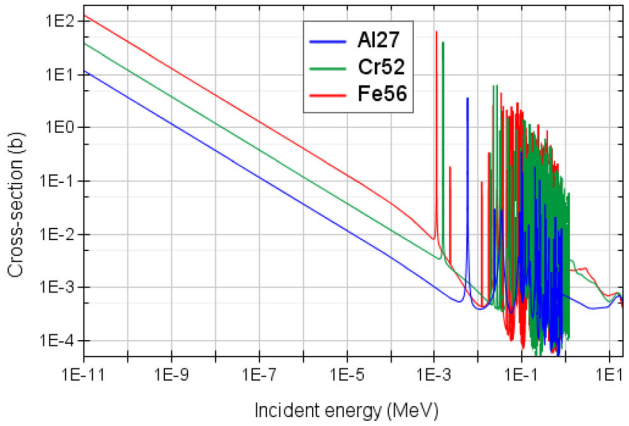

Fig. 21 (Color online) Radiative neutron capture cross sections of ^{56}Fe, ^{52}Cr, and ^{27}Al. The data are from the JEFF-3.1.1 nuclear data library [8]

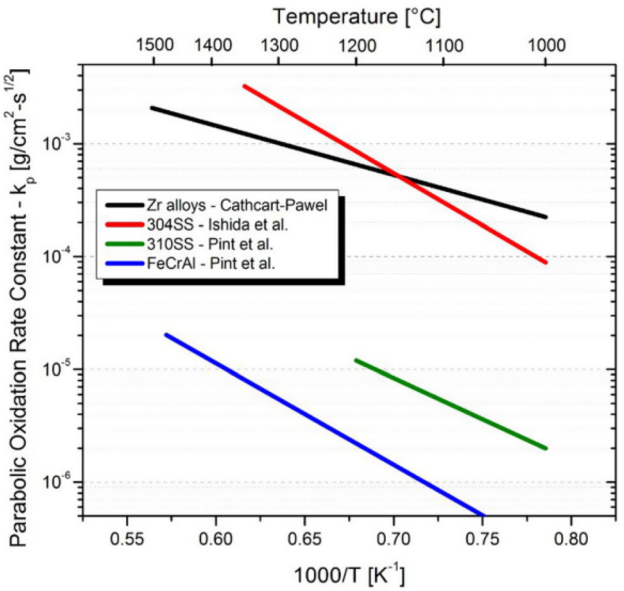

Fig. 22 (Color online) Oxidation kinetics of a zircaloy and three SSs. The figure is from Ref. [114]

The corresponding neutron- and photon-induced irradiation damage can be calculated using the methods presented in Refs. [117–121].

Commercial FeCrAl contains 20 wt% Cr and 5 wt% Al. Reducing the Cr content can improve the irradiation resistance by reducing the amount of Cr-rich α' precipitates [122, 123]. The high-temperature oxidation behaviors of different types of low-Cr FeCrAl alloys were investigated [124]. The melting points of different low-Cr FeCrAl alloys vary from 1525 to 1543 °C [125] and are slightly higher than that of the commercial FeCrAl (1500 °C) [7]. However, as indicated by the effects of the Cr and Al alloy contents on the steam oxidation resistance at 1473 K

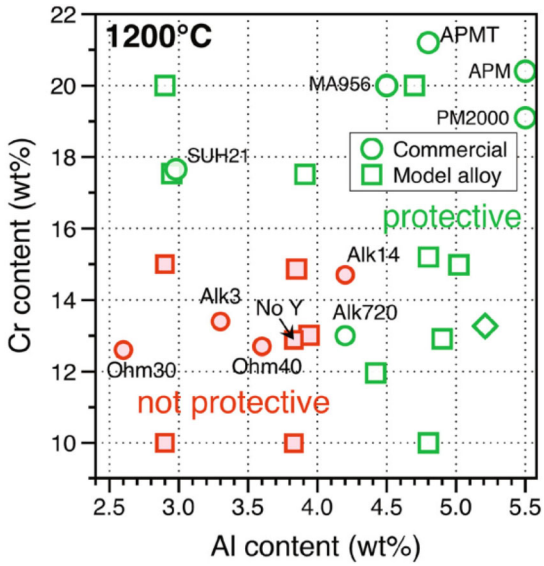

Fig. 23 (Color online) Effects of the Cr and Al alloy contents on the steam oxidation resistance at 1473 K. "Protective" (open green symbols) corresponds to the slow growth of alumina over 4 h in steam, and "not protective" (square red symbols) corresponds to an oxidation resistance similar to that of 304SS (shown in Fig. 21). The figure is from Ref. [126]

shown in Fig. 23 [126], lower Cr and Al contents correspond to a lower oxidation resistance [111, 112].

The thermal conductivity of FeCrAl is not so different from the current zircaloy. Figure 24 presents the thermal conductivities of FeCrAl and Zr-4. The thermal conductivity of Zr-4 is based on Eq. (2), and that of the zircaloy is the value recommended by the IAEA. The systematics of the thermal conductivity as a function of the temperature T (in units of K) were presented by Qiu et al. [127] as

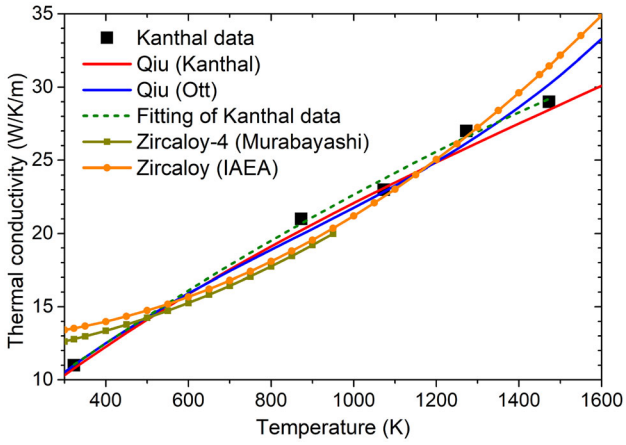

Fig. 24 (Color online) Thermal conductivity of FeCrAl in comparison with those of Zr-4 and zircaloy. The discrete data are from Ref. [128]. The systematics of FeCrAl were presented by Qiu et al. [127]

$$\lambda_{\mathrm{FeCrAl,K}}(T) = 3.72 + 0.024T - 7.2 \times 10^{-6}T^2 + 1.56573 \times 10^{-9}T^3 \quad (16)$$

$$\lambda_{\mathrm{FeCrAl,O}}(T) = 2.993 + 0.03T - 1.8429 \times 10^{-5}T^2 + 7.1965 \times 10^{-9}T^3 \quad (17)$$

for the APMT FeCrAl manufactured by Kanthal [128] and the FeCrAl material studied by Ott et al. [114]. Notably, the thermal conductivity of AMPT given by Kanthal [128] can be described by the following second-order polynomial:

$$\lambda_{\mathrm{AMPT}}(T) = 4.56 + 0.021T - 2.9 \times 10^{-6}T^2, \quad (18)$$

where T represents the temperature (in K). This polynomial fitting is represented by the green dashed curve in Fig. 24.

Figure 25 shows the peak cladding temperature (PCT) of UO_2 fuel combined with zircaloy and FeCrAl claddings under a large-break LOCA condition with low-pressure coolant injection (LPCI) starting 91 s after the break [114]. The approximately 75-K difference in the maximum temperature between the two systems is mainly due to the higher specific heat of FeCrAl. Therefore, although the thermal conductivity of FeCrAl is close to that of the current zircaloy, the higher specific heat can increase the margin for cladding melting or delay the cladding melting.

In addition to a higher specific heat, FeCrAl has improved mechanical strength than the current zircaloy for temperatures up to 1300 °C [114]. Additionally, it has a better irradiation resistance than the zircaloy [114]. For example, the irradiation growth observed in Zr alloys [129] is not expected in austenitic steel [130, 131]. This is confirmed by Ref. [132]. Moreover, FeCrAl has excellent corrosion resistance in both PWR and BWR coolant environments [133].

Compared with the zircaloy, SSs (including FeCrAl) have a significantly larger thermal neutron absorption cross

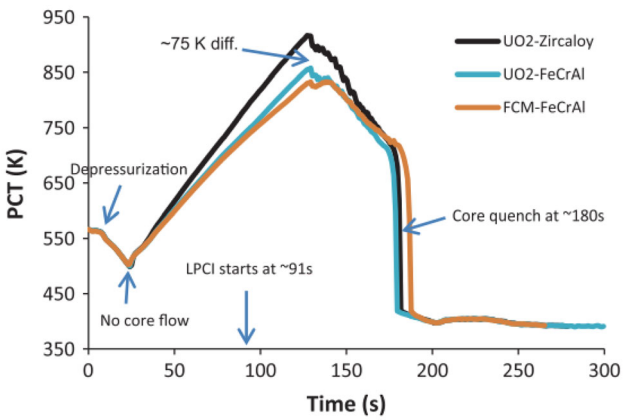

Fig. 25 (Color online) PCT under the large-break LOCA condition with LPCI starting 91 s after the break. The figure is from Ref. [114]

section, which reduces their neutron economy. To compensate for the negative reactivity of FeCrAl, higher U density fuels, such as UN and U_3Si_2, and/or higher ^{235}U enrichment fuels can be used together with FeCrAl. Another challenge of using FeCrAl is the release of tritium into the coolant, because it does not react with H_2 to form stable hydrides as in the case of the zircaloy [7]. This issue may be resolved by the addition or formation of alumina on the inner or outer surface of the cladding [134]. It is also possible to use other tritium barriers that are developed for fusion reactors [135].

4.2.2 SiC and SiC/SiC

The SiC ceramic was initially proposed to be used in fusion reactors and is now also considered as an enhanced ATF-cladding material. SiC has excellent high-temperature properties, a high irradiation resistance, low activity, and a small thermal neutron absorption cross section. The main issue for the nuclear application of SiC is the ductile feature of the ceramic. To improve the properties of SiC for nuclear applications, the following four nuclear-grade SiC materials are proposed [136].

(1) Simple continuous SiC fiber-reinforced SiC matrix composites [137–140], which are denoted as SiC_f/SiC or SiC/SiC: Two crucial issues associated with SiC_f/SiC are hydrothermal corrosion and the low retention capacity of fission products [141, 142].
(2) Two-layered ceramic cylinders [143, 144], as shown in Fig. 26a: The inner SiC_f/SiC is designed to withstand the peak mechanical and swelling-induced tensile stresses, while the outer monolith layer protects against the reaction with steam.
(3) Duplex SiC cladding design [145, 146], as shown in Fig. 26b: The inner SiC is designed to enclose the radiative fission products, and the outer layer provides additional strength to the cladding.
(4) Triplex SiC cladding design [143, 145, 147], as shown in Fig. 26c: This is based on the duplex design, with an additional 50–150-μm-thick environmental barrier coating that provides additional protection from corrosion.

The thermal conductivity of nonirradiated SiC depends on the fabrication process. Figure 27a summarizes the thermal conductivity of different types of SiC [148]. The analytical fitting shown in Fig. 27 is expressed as follows [148]:

$$\lambda_{SiC}(T) = \left(-0.0003 + 1.05 \times 10^{-5} T\right)^{-1}, \quad (19)$$

where T represents the temperature (in K). Notably, the thermal conductivity of SiC is significantly reduced by neutron irradiation [149]. Figure 27b presents the thermal conductivity of SiC irradiated at different temperatures with respect to the fast neutron fluence [148]. As shown, a higher irradiation temperature leads to a higher room-temperature thermal conductivity of SiC. The changes in the thermal conductivity due to irradiation were studied in detail [150].

SiC can be oxidized by steam water by the following chemical reaction at a temperature higher than approximately 1100 °C:

$$SiC + 3H_2O \rightarrow SiO_2 + 3H_2 + CO. \quad (20)$$

Thus, the oxidation of SiC in steam produces both H_2 and CO. However, the oxidation rate of SiC is significantly lower than that of the zircaloy. As shown in Fig. 28, the parabolic oxidation rate constant of SiC is approximately

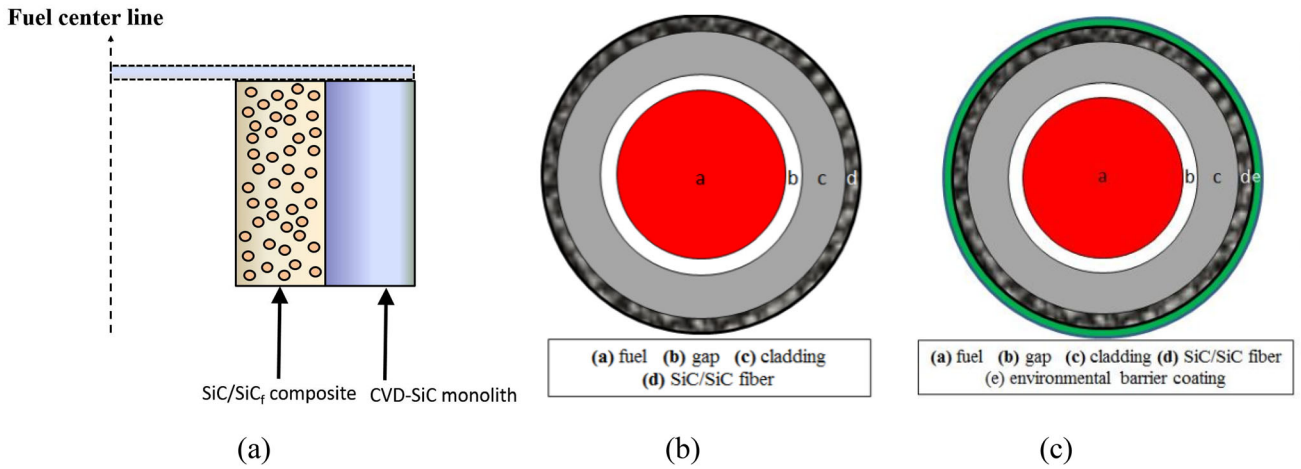

Fig. 26 (Color online) Different designs of nuclear-grade SiC. **a** Multilayer SiC (figure is from Ref. [144]); **b** duplex SiC cladding design (figure is from Ref. [145]); **c** triplex SiC cladding design (figure is from Ref. [145])

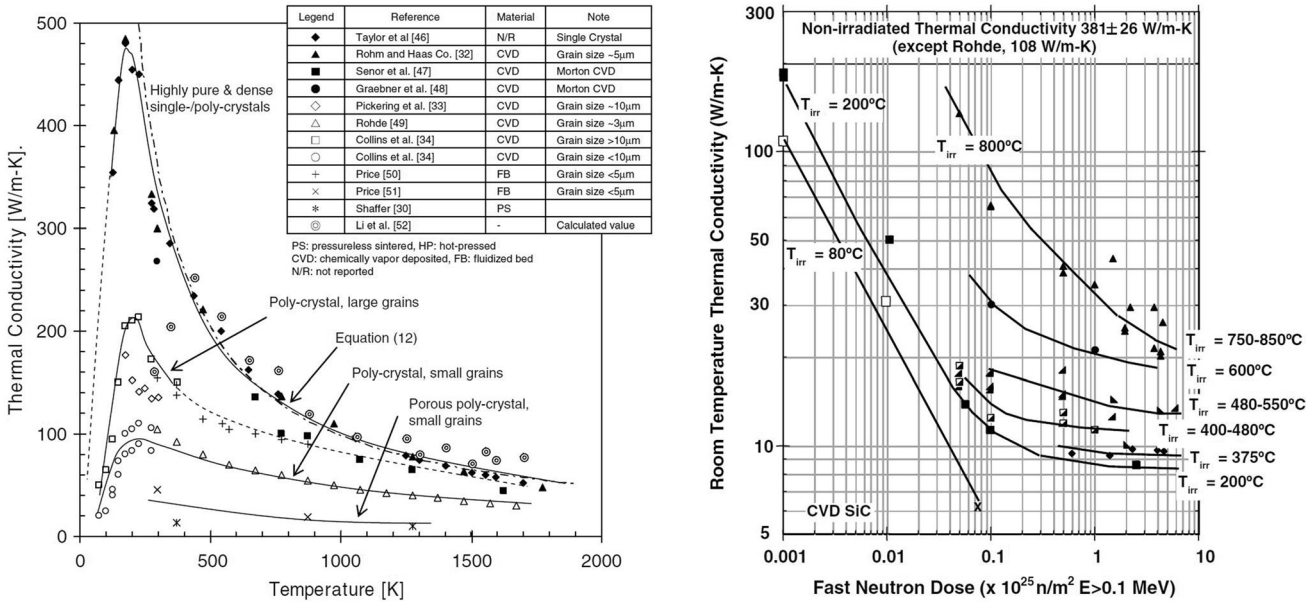

Fig. 27 Thermal conductivity for different types of nonirradiated monolithic SiC with respect to the temperature (left) and the fast neutron fluence at room temperature (right). The figures are from Ref. [148]

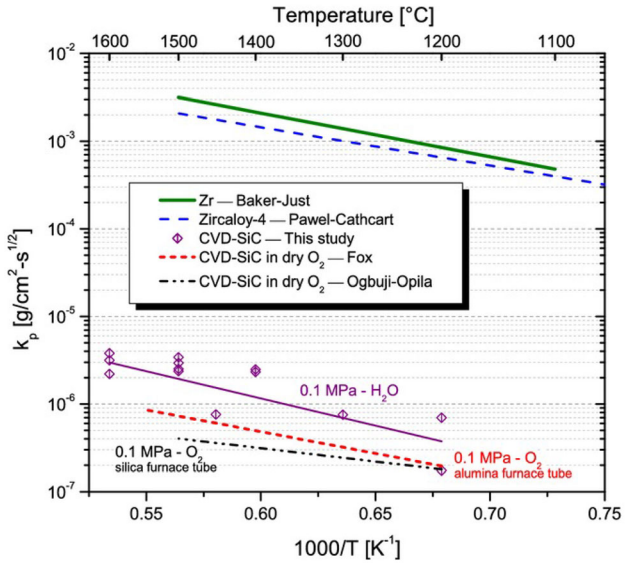

Fig. 28 (Color online) Oxidation kinetics of the zircaloy and SiC. The figure is from Ref. [151]

three orders of magnitude smaller than that of the zircaloy. Comparing Figs. 21 and 28 reveals that the oxidation rate of SiC is lower than that of FeCrAl. Consequently, SiC has a better oxidation resistance under accident conditions than the zircaloy and FeCrAl.

Recently, a CEA team investigated the chemical compatibility of SiC with UO_{2+x} [152]. It was found that rare chemical reaction occurs between SiC and UO_{2+x} at temperatures up to 1514 K. Notably, CO gas was observed between 1450 and 1970 K. Additionally, a liquid phase formed between 1850 and 1950 K in the UO_{2+x}/SiC system.

5 Neutronic studies on alternative fuel-cladding systems

The neutronic performance is a critical feature of nuclear reactors. Therefore, neutronic studies are of great importance for new fuel and cladding designs. The neutronic evaluations of different fuel-cladding systems are summarized in this section.

5.1 Current system using coated zircaloy cladding

In general, because the coating is thin compared with the 570-μm-thick zircaloy cladding, the neutronic behaviors of the zircaloy with a coating are similar to those of the current UO_2–zircaloy system. Examples of the fuel temperature coefficient (FTC; also called the Doppler coefficient), the moderator temperature coefficient (MTC), and the void reactivity coefficient (VRC) with 5% (VRC05) and 90% (VRC90) coolant leakage for 50-μm-thick coatings at the BOL and EOL are presented in Table 7 [153]. The quantitative data in Table 7 confirm that the neutronic behaviors of the coated zircaloy are similar to those of the current zircaloy cladding.

The main change in the neutronic characteristics of the coated zircaloy cladding is the reactivity loss due to the increase in neutron absorption caused by the coating materials. Figure 29 shows the additional ^{235}U enrichment

Table 7 Reactivity coefficients for a PWR with 50-μm coatings, calculated by Younker and Fratoni [153]

	Coating	FTC (pcm/K)	MTC (pcm/K)	VRC05 (pcm/%)	VRC90 (pcm/%)
BOL	Ti_3AlC_2	1.14 ± 0.07	30.74 ± 0.66	101.33 ± 1.33	483.45 ± 0.18
	Ti_2AlC	1.03 ± 0.07	30.20 ± 0.66	102.04 ± 1.33	483.88 ± 0.18
	Nb_2AlC	1.17 ± 0.07	32.82 ± 0.66	104.95 ± 1.32	507.72 ± 0.18
	TiAlN	1.17 ± 0.07	32.80 ± 0.66	103.26 ± 1.33	485.27 ± 0.18
	Zr-4	1.08 ± 0.06	29.73 ± 0.65	99.45 ± 1.31	488.43 ± 0.17
	Ref.	1.12 ± 0.06	29.49 ± 0.65	96.86 ± 1.30	481.80 ± 0.17
EOL	Ti_3AlC_2	2.21 ± 0.23	75.80 ± 2.30	245.70 ± 4.61	976.43 ± 0.67
	Ti_2AlC	2.94 ± 0.23	79.52 ± 2.29	250.96 ± 4.61	976.33 ± 0.66
	Nb_2AlC	2.43 ± 0.23	78.58 ± 2.29	253.96 ± 4.60	1019.6 ± 0.71
	Ti_3AlC_2	2.29 ± 0.23	71.69 ± 2.29	244.17 ± 4.61	979.49 ± 0.67
	Zr-4	2.30 ± 0.23	73.04 ± 2.27	242.04 ± 4.55	990.31 ± 0.67
	Ref.	2.54 ± 0.23	73.46 ± 2.18	241.46 ± 4.54	987.11 ± 0.69

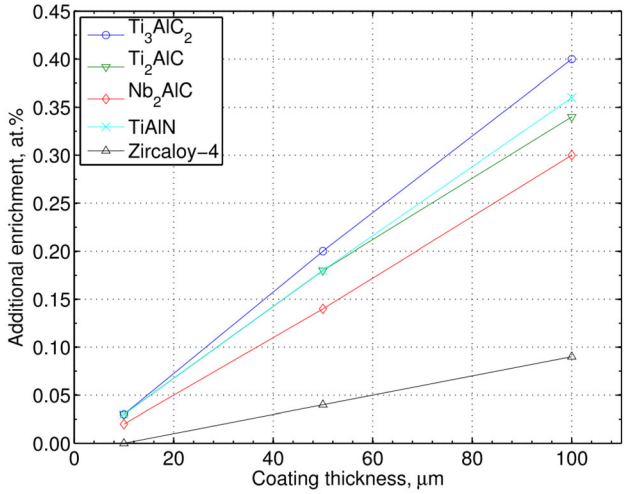

Fig. 29 (Color online) Additional ^{235}U enrichment in UO_2 fuel to compensate for the anti-reactivity induced by the coating materials by keeping the cycle length equal to that of the current UO_2–Zr-4 system. The figure is from Ref. [153]

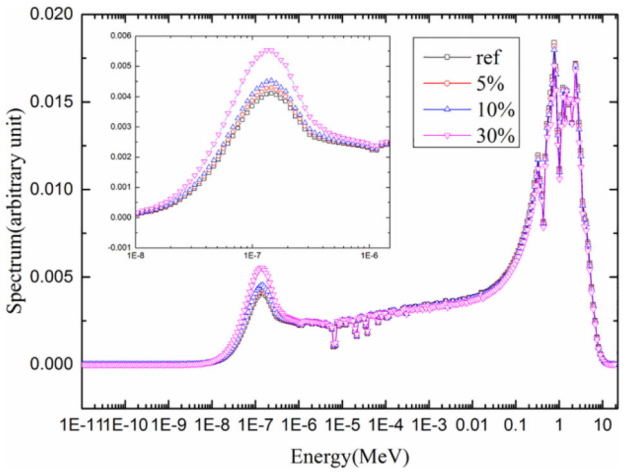

Fig. 30 (Color online) Neutron flux spectra of the UO_2–BeO–Zr-4 system with the incorporation of different amounts of BeO at the BOL. The figure is from Ref. [155]

in the UO_2 fuel needed to compensate for the anti-reactivity induced by the coating materials by keeping the cycle length equal to that of the current UO_2–Zr-4 system [153]. The anti-reactivity induced by the additional coating depends on the materials and the thickness of the coating. However, because the coating materials typically have higher mechanical strength than the zircaloy, the addition of the coating may allow the thickness of the zircaloy to be reduced. Consequently, the necessary increase in ^{235}U enrichment should be smaller than that shown in Fig. 29. Moreover, if fuel with higher U density is used, the importance of the negative reactivity induced by the coating materials decreases.

5.2 UO_2–BeO fuel and zircaloy cladding system

Compared with the current UO_2–Zr-4 system, the doping of BeO into UO_2 fuel reduces the cycle length if the same ^{235}U enrichment is used. Smith reported that the cycle length was reduced by approximately 2 and 3 d with the addition of 5 and 10 vol% BeO, respectively, for an 18-month cycle length design [86]. The increases of the U enrichment for different amounts of BeO doping are presented in Ref. [154].

As an example at the BOL given in Fig. 30, Refs. [86, 155] show that the addition of BeO to the UO_2 fuel leads to the softening of the neutron flux spectrum. This is the main reason why the control rod worth is higher for the UO_2–BeO fuel than that for the current UO_2 fuel. However, as shown in Fig. 31, Smith reported that a higher B concentration is required with BeO doping to maintain the core

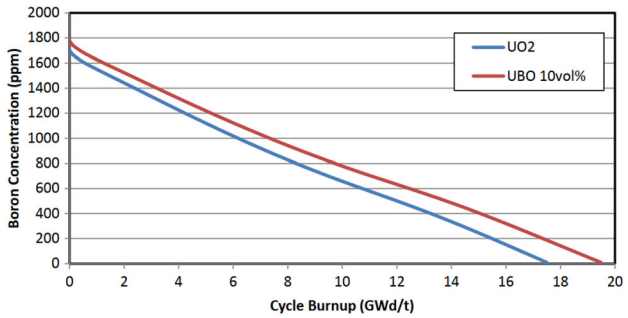

Fig. 31 (Color online) Critical B concentration for the current UO_2 fuel and 10 vol% BeO-doped fuel. The figure is from Ref. [86]

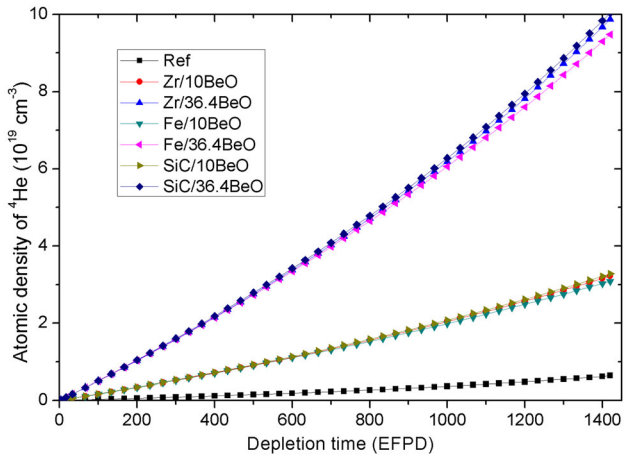

Fig. 32 (Color online) Atomic density of ^{4}He produced in the fuel for different cases with the same cycle length, including the reference case and UO_2–(x vol%)BeO (x = 10, 36.4) fuel with zircaloy, FeCrAl, and SiC claddings [154]

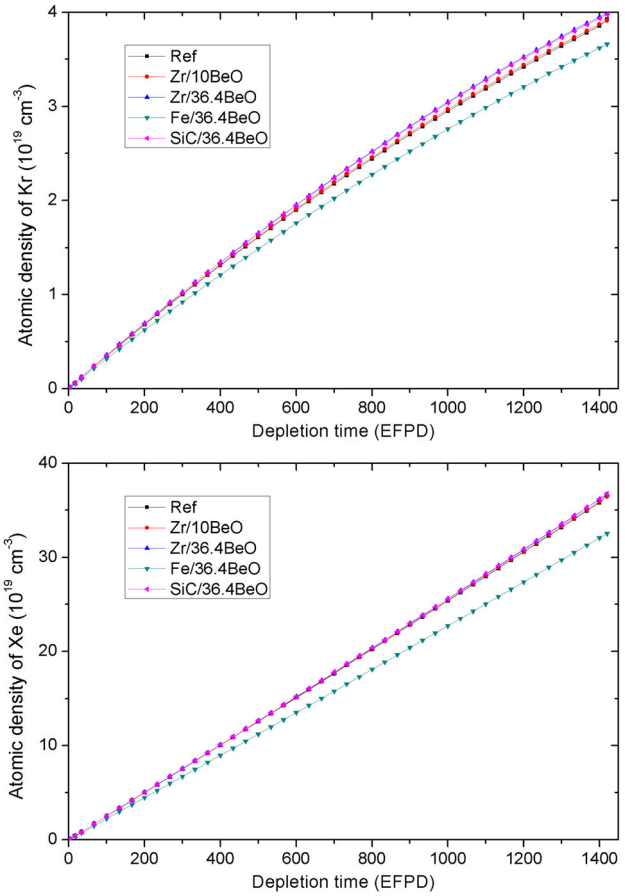

Fig. 33 (Color online) Atomic density of Kr and Xe produced in the fuel for different cases with the same cycle length, including the reference case, UO_2–(x vol%)BeO (x = 10, 36.4) fuel with a zircaloy cladding, and UO_2–(36.4 vol%)BeO fuel with FeCrAl and SiC claddings [154]

under the critical condition [86]. Notably, the critical B concentration depends on the U enrichment.

Figure 32 shows the ^{4}He production for the reference UO_2–Zr-4 system and different UO_2–BeO fuels with zircaloy, FeCrAl, and SiC claddings. As explained in Sect. 4.1.1, the incorporation of BeO leads to significant ^{4}He production. Nevertheless, as the concentrations of Kr and Xe shown in Fig. 33, the gas production of Kr and Xe is similar between the UO_2 and UO_2–BeO fuels. Because the production of Xe is far more important than that of Kr and He, the contribution of BeO to the total gas production is limited. However, because the independent variable in Figs. 32 and 33 is the number of EFPDs, similar gas production on the same EFPD implies less gas production at the same burnup level for greater BeO doping (the same power with a smaller U mass). This conclusion agrees with Ref. [87], in which less fission gas release was observed in UO_2–BeO fuel compared with UO_2 fuel at a given burnup level.

Figure 34 (upper panel) shows the radial power distribution for 10 and 36.4 vol% BeO at the BOL, middle of life (MOL), and EOL [154]. The radial power distribution is flatter with the incorporation of larger amounts of BeO. Because the thermal conductivity of UO_2–BeO increases with the fraction of BeO and the radial power distribution is flatter for greater BeO doping, the radial fuel temperature is significantly flatter for UO_2–BeO fuel doped with a larger amount of BeO. On the other hand, for the UO_2–(36.4 vol%)BeO fuel, as shown in Fig. 34 (lower panel) [154], the radial power distribution is not sensitive to the cladding material. Thus, the radial temperature distribution is mainly determined by the cladding material, which affects the temperature at the surface of the fuel pellet.

5.3 UN fuels and zircaloy cladding system

Because UN fuel has a significantly higher U density than UO_2 fuel, the moderator-to-fuel ratio of UN-based fuel is lower than the typical value ($\sim$ 2) for the UO_2–Zr system if the geometric design and the fuel assembly are not changed. Therefore, the MTC of UN-based fuel is more

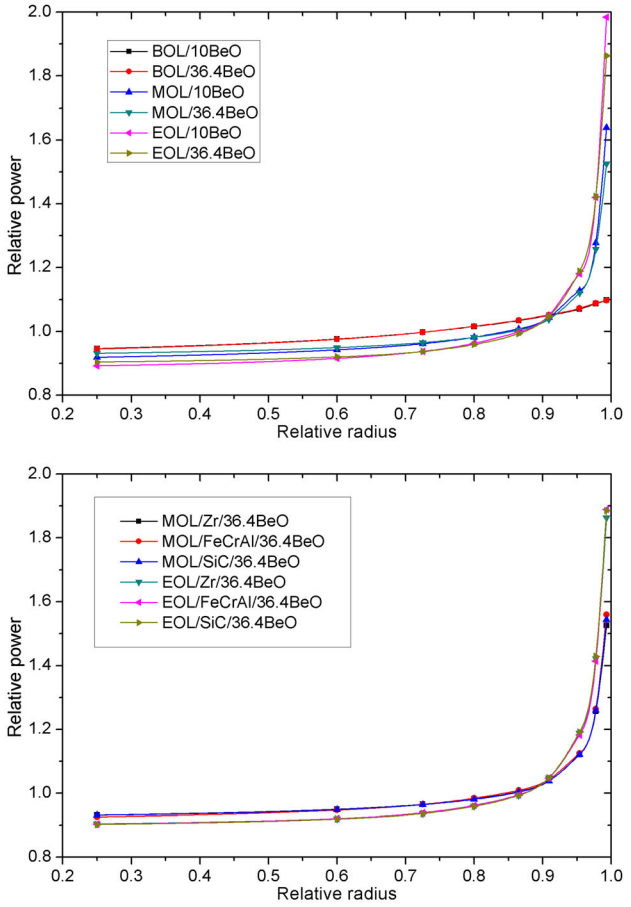

Fig. 34 (Color online) Radial power distribution in UO_2–(x vol%)-BeO (x = 10, 36.4) fuel with a zircaloy cladding at the BOL, middle of life (MOL), and EOL (upper) and in UO_2–(36.4 vol%) BeO fuel with zircaloy, FeCrAl, and SiC claddings at the MOL and EOL (lower) [154]

negative than that of the current UO_2 fuel. This was verified by Brown et al., who calculated the MTCs of different UN-based fuels and UO_2 fuel, as shown in Fig. 35 [156]. The enhanced moderator feedback can be considered as an improved inherent safety feature of UN-like high U density fuels.

Owing to the decrease in the moderator-to-fuel ratio compared with that for the UO_2 fuel, the neutron flux spectra for the UN-based fuel are hardened. The hardening of the neutron spectrum of the UN-based fuel is confirmed by Ref. [156] and is shown in Fig. 36. A direct consequence of the hardening of the neutron spectrum is a decrease in the B and control rod worth, as shown in Fig. 37 [156]. Therefore, the control system should be redesigned for UN-based fuel.

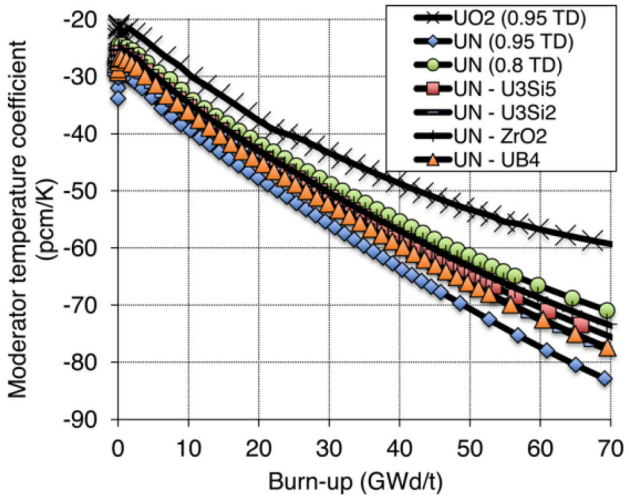

Fig. 35 (Color online) MTCs of UN-based fuels and UO_2 fuel at the BOL. "TD" represents "theoretical density." The figure is from [156]

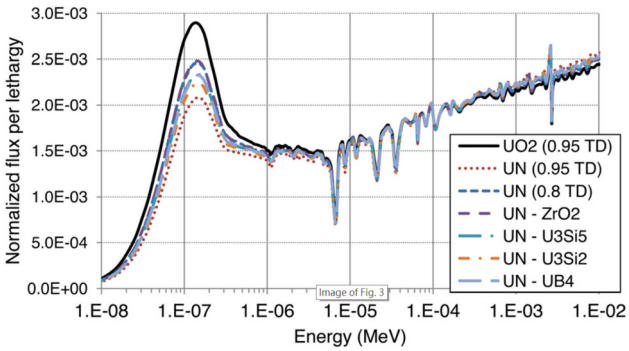

Fig. 36 (Color online) Neutron flux spectra of UN-based fuels and UO_2 fuel at the BOL. "TD" represents "theoretical density." The figure is from Ref. [156]

5.4 U_3Si_2–FeCrAl system

U_3Si_2–FeCrAl systems have a different neutronic performance from the current UO_2–Zr-4 system because of the different moderator-to-U ratios and different thermal absorption cross sections of the claddings. Consequently, neutronic studies are important and fundamental for the U_3Si_2–FeCrAl system.

Figure 38 presents the infinite multiplication factor (k_{inf}) for 4.9%-enriched U_3Si_2 fuel with FeCrAl claddings of different thicknesses, as well as the current UO_2–Zr-4 system (^{235}U enrichment is 4.9% in the "Ref." case) [14]. At the BOL, the reactivity of the U_3Si_2–FeCrAl system is lower than that of the UO_2–Zr-4 system because (1) FeCrAl has a larger thermal neutron absorption cross section than the zircaloy and (2) the higher U density in U_3Si_2 (and larger volume of fuel for a cladding thickness of < 571.5 μm) leads to a lower moderator-to-U ratio. The decrease in k_{inf} with the increasing EFPD is smaller for the

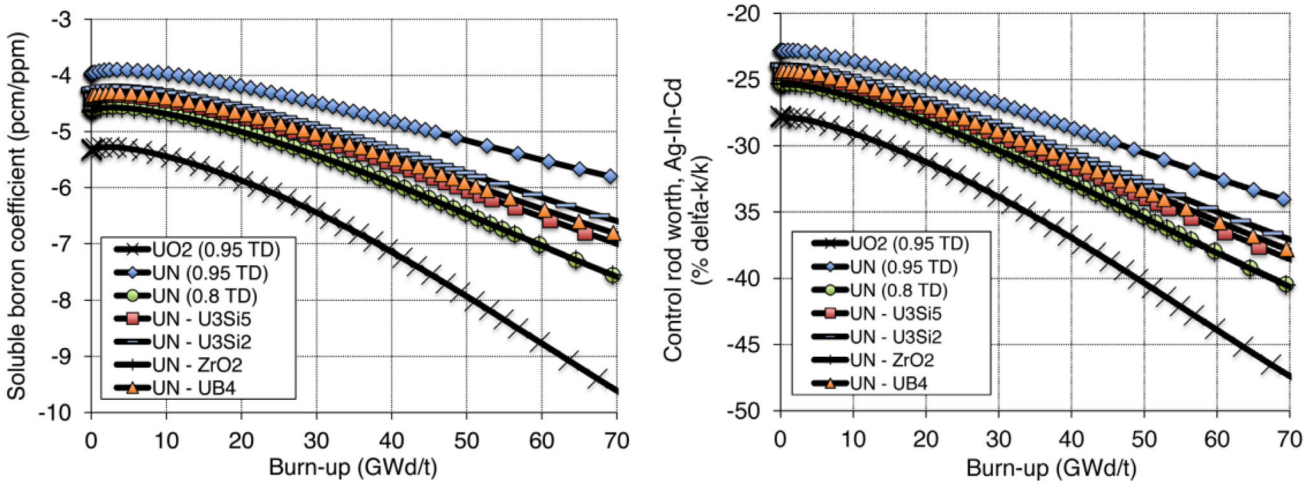

Fig. 37 (Color online) Efficiency of B (left) and the control rod (right) for UN-based fuels and UO_2 fuel. The figures are from Ref. [156]

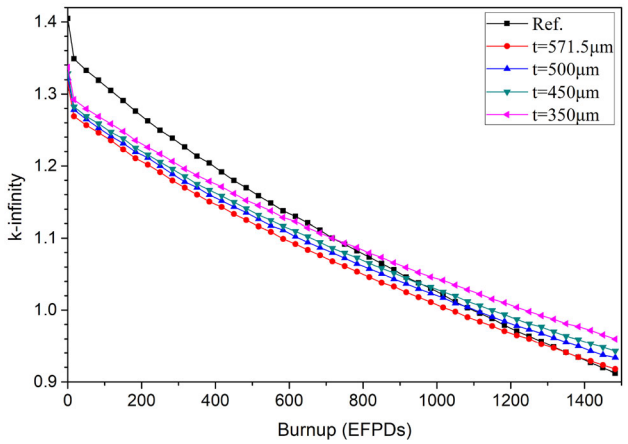

Fig. 38 (Color online) k_{inf} versus burnup for 4.9%-enriched U_3Si_2 fuel with FeCrAl claddings of different thicknesses [14]

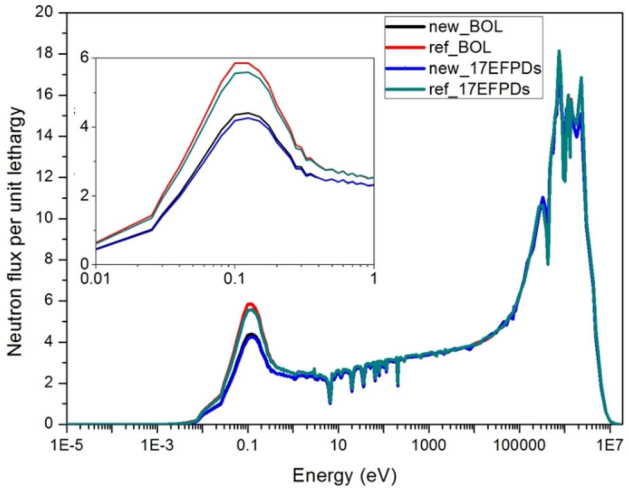

Fig. 39 (Color online) Neutron flux spectra of the current UO_2–Zr-4 system and the 4.9%-enriched U_3Si_2 fuel with 450-μm-thick FeCrAl (denoted as "new") at the BOL and the first step of the depletion calculation (17 EFPDs) [14]

U_3Si_2–FeCrAl systems because of (1) the larger amount of ^{239}Pu production [14] and (2) the lower burnup level (the same power production but more U).

Even if the k_{inf} at the BOL is smaller for U_3Si_2–FeCrAl systems, this does not imply that a lower B concentration is needed to maintain the reactor core under the critical condition. In fact, similar to the hardening of the neutron spectrum (as shown in Fig. 39 [14]) due to the larger thermal neutron capture cross section of FeCrAl than that of zircaloy [14, 156–158], the B is less efficient for providing a negative reactivity. Salazar et al. reported that the critical B concentration of the U_3Si_2–FeCrAl system is higher than that of the UO_2–Zr-4 system for an 18-month cycle length I^{2}S-LWR design [159].

Because the U_3Si_2 fuel has a higher U density than the UO_2 fuel, it can compensate for the negative reactivity induced by FeCrAl. The relationship between the ^{235}U enrichment (e, in %) and the FeCrAl thickness (t, in μm) is expressed as follows (for the same cycle length as the current Westinghouse 24-month cycle UO_2–Zr-4 system) [14]:

$$e = 3.2 \times 10^{-3} t + 3.5. \quad (21)$$

Assuming that the thickness of the steel is 350 μm (this value has been historically used) [109], the critical ^{235}U enrichment is 4.58%. The gain of the fuel enrichment allows the U_3Si_2–FeCrAl system to transmute long-lived minor actinides [160]. If the 4.9% enrichment is used for the U_3Si_2–FeCrAl system, the critical cladding thickness is 450 μm. This combination was referred to as the "new fuel-cladding combination" in our previous work and is denoted as "new" in the figures.

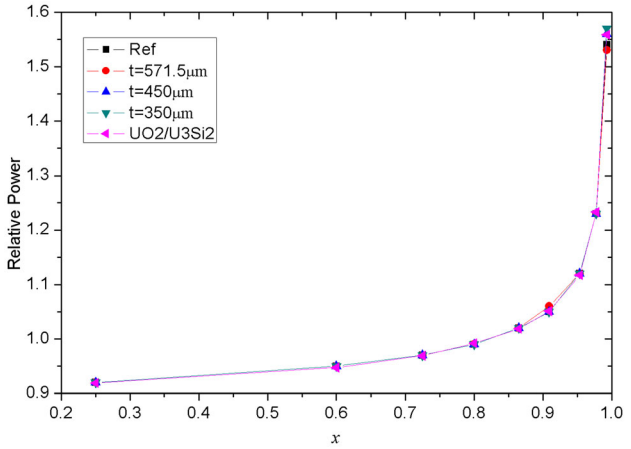

Fig. 40 (Color online) Radial power distribution of the current UO_2–Zr-4 system, three U_3Si_2–FeCrAl systems, and a combined UO_2/U_3Si_2–FeCrAl system with a 24-month cycle length at 500 EFPDs [161]

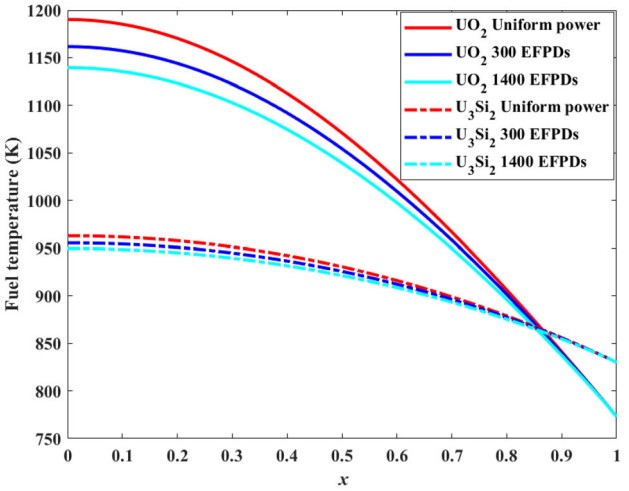

Fig. 41 (Color online) Fuel temperature distribution for UO_2 and U_3Si_2–(571.5 μm)FeCrAl with temperatures of 773 and 830 K, respectively, at the fuel outer surface [161]

For example, at 500 EFPDs, as shown in Fig. 40 [161], the radial power distributions in the fuel pellets of the current UO_2–Zr-4 system and three U_3Si_2–FeCrAl combinations with critical ^{235}U enrichment determined by Eq. (21) are close to each other [161]. Moreover, with the same cycle length, the hybrid UO_2/U_3Si_2 fuel with the FeCrAl cladding has a similar radial power distribution to the four aforementioned scenarios, as a function of EFPD [161]. The following second-order polynomial can fit the radial power distribution as a function of the fuel exposure (s) [161]:

$$f(x,s) = a(x)s^2 + b(x)s + c(x), \tag{22}$$

where x represents the normalized radial distribution, and the coefficients a, b, and c can be expressed in the following form [73]:

$$g(x) = A\exp(B(1-x)) + C\exp(D(1-x)) + E. \tag{23}$$

Here, A, B, C, D, and E are constants determined by fitting simulated data.

The use of a nonuniform radial power distribution reduces the peak fuel temperature because of the relatively high thermal power density at the periphery of the fuel pellet. This is confirmed in Fig. 41 [161], in which the periphery phenomenon becomes more important from low burnup to high burnup and from a uniform power distribution to a realistic nonuniform radial power distribution. Additionally, because the thermal conductivity of U_3Si_2 is higher than that of UO_2 (see Fig. 15), similar radial power distributions imply a flatter radial temperature distribution in the U_3Si_2 fuel.

Even if the 571.5-μm-thick FeCrAl leads to an approximately 60 K higher temperature at the surface of the fuel pellet compared with the zircaloy cladding [162], the centerline temperature in the U_3Si_2 fuel is approximately 200 K lower than that in the UO_2 fuel [161]. If a thinner FeCrAl cladding is used (e.g., 450 μm, as proposed in Ref. [14], or the historically used thickness of 350 μm [109]), the fuel temperature is lower for the U_3Si_2–FeCrAl combination. Moreover, our recent study indicated that the use of a dual-coolant annular fuel rod can significantly reduce the fuel temperature of U_3Si_2–FeCrAl systems [163].

Figure 42 shows the FTCs and MTCs of the current UO_2–Zr-4 system and the new U_3Si_2–FeCrAl system [14]. The FTCs and MTCs of the two systems are close at < 200 EFPDs. In general, the absolute values of the FTC and MTC for the U_3Si_2–FeCrAl system are slightly smaller than those for the UO_2–Zr-4 system at > 200 EFPDs. Consequently, the U_3Si_2–FeCrAl system has slightly less inherent safety than the current UO_2–Zr-4 system.

Reference [14] compares the VRC of the two systems in the cases of 5% and 50% void of the moderator. The behaviors of the VRC are similar to those of the MTC, because both the increase in the moderator temperature and the loss of coolant lead to the reduction of the amount of moderator. Therefore, the inherent safety of the U_3Si_2–FeCrAl system under the LOCA accident condition is slightly lower than that of the current UO_2–Zr-4 system from the view point of reactivity feedback.

The control rod worths of the two systems are presented in Fig. 43 [14]. As shown, the control rod is less effective for U_3Si_2–FeCrAl owing to the hardening of the neutron spectrum. Consequently, a new control system design, including the control rods and B-concentration control, is required for the U_3Si_2–FeCrAl fuel-cladding system.

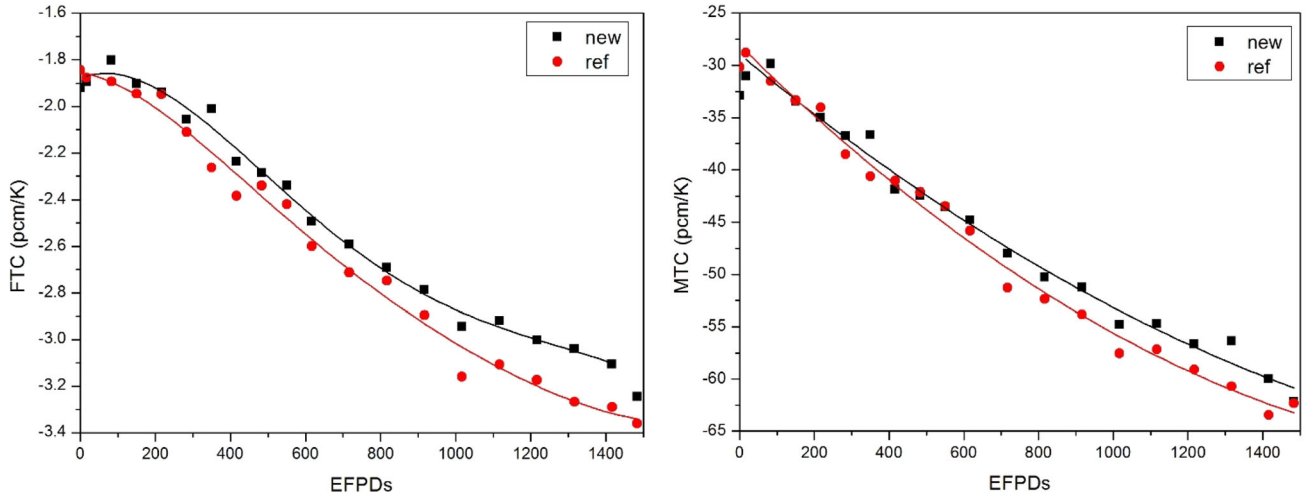

Fig. 42 (Color online) FTCs (left) and MTCs (right) of the current UO_2–Zr-4 system and the new U_3Si_2–FeCrAl system [14]

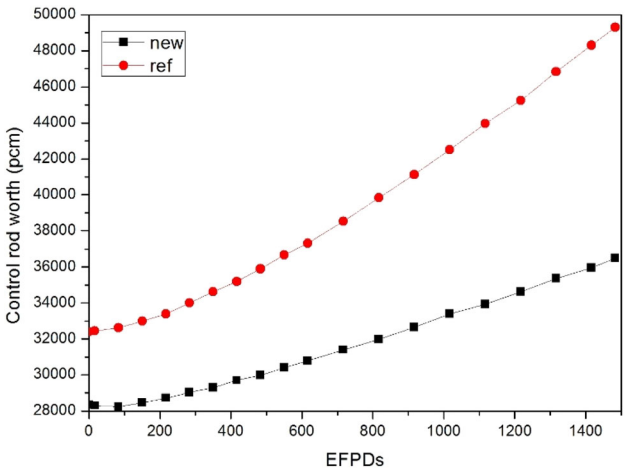

Fig. 43 (Color online) Integrated control rod worth for an assembly of the current UO_2–Zr-4 system and the new U_3Si_2–FeCrAl system [14]

5.5 Comparison of alternative systems with current fuel-cladding system

This subsection briefly summarizes the neutronic features of different fuel-cladding systems compared with the current UO_2–Zr-4 fuel-cladding system. Table 8 presents the hardening and the softening of the neutron flux spectrum, the efficiency of reactivity control, and the cycle length.

The hardening of the neutron spectrum for UO_2 fuel with the coated zircaloy cladding has not been studied in detail. However, because the coating materials have larger thermal neutron absorption cross sections than the zircaloy, slight hardening of the neutron spectrum is expected. The neutron spectra of the other three cases are already presented in the corresponding detailed analyses. For the same control materials, the efficiency of the reactivity control is mainly determined by the neutron flux spectrum. Therefore, the reactivity control is more efficient for a softer neutron spectrum. More efficient reactivity control does not necessarily imply a more accessible control system. For example, UO_2–BeO fuel has a softer neutron spectrum than UO_2 fuel (as shown in Fig. 30), but the former requires a

Table 8 Neutronic features of different alternative fuel-cladding systems compared with the current fuel-cladding system

System	Effect on neutron spectrum	Efficiency of reactivity control[a]	Cycle length[b]
UO_2 fuel with coated zircaloy cladding	Hardening	Less efficient	Shorter
UO_2–BeO fuel and zircaloy cladding	Softening	More efficient	Shorter
UN fuel and zircaloy cladding	Hardening	Less efficient	Longer
U_3Si_2 fuel and FeCrAl cladding	Hardening	Less efficient	Shorter

[a]The efficiency of reactivity control depends on the neutron flux spectrum. More efficient reactivity control does not necessarily imply a more accessible control system

[b]The cycle length depends on the fuel enrichment and cladding thickness. Here, we consider cases with the same fuel enrichment and cladding thickness

higher B concentration to maintain the critical condition (as shown in Fig. 31) because of its higher reactivity.

The cycle length is one of the most important characteristics affecting the neutron economy of a fuel-cladding system. It depends on the fuel enrichment, cladding thickness, operational history, etc. We compare the cycle lengths of different alternative fuel-cladding systems with that of the current UO_2–Zr-4 fuel-cladding system, assuming the same fuel enrichment and cladding thickness and neglecting other factors, such as the operational history. A shorter cycle length is expected for UO_2 fuel with the coated zircaloy cladding, owing to the additional neutron absorption provided by the coating materials. This applies to both the UO_2–BeO fuel and the zircaloy cladding system, because the doping of BeO leads to a smaller amount of U. In contrast, UN fuel with the zircaloy cladding has a longer cycle length than the current UO_2–Zr-4 system, because of the higher U density in the fuel.

There is a compensation in the U_3Si_2 fuel and FeCrAl cladding system, because the fuel has a higher U density and the cladding has a larger thermal neutron absorption cross section than the current system. Numerical results indicate that the U_3Si_2–FeCrAl combined system has a shorter cycle length than the UO_2–Zr-4 system if the same fuel enrichment and cladding thickness are used. However, because of the better mechanical performance of FeCrAl compared with the zircaloy, a significantly thicker cladding is possible. If 350-μm-thick steel (historically used [109]) is employed, the critical ^{235}U enrichment is 4.58%. If 4.9% enrichment (as for the reference UO_2–Zr-4 system) is used, the critical cladding thickness is 450 μm for the U_3Si_2–FeCrAl system.

6 Summary

To improve the accident tolerance of the nuclear fuel-cladding system in LWRs, extensive studies on the enhanced ATF have been performed after the Fukushima accident. In this review, we discussed the features of the current UO_2–Zr system, including the optimized neutron economy, the thermal conductivity of the UO_2 fuel, and the main challenges for the zircaloy cladding. Then, we summarized different technologies that can improve the fuel performance under normal and accident conditions.

For protecting the cladding from the chemical reaction of Zr with water, a surface-modified Zr-based cladding is proposed for improving the oxidation resistance of the fuel cladding. We introduced different coating technologies, including metallic coatings, nonmetallic coatings, ceramic coatings, and the ODS coating. Numerous coating technologies have been developed by different laboratories. In addition to the coating technology, the implantation of several ions, such as Al, for increasing the oxidation resistance of the zircaloy is a feasible short-term solution to improve the accident tolerance of the fuel cladding.

Because the technology of the zircaloy has been well optimized in the past seven decades, it is difficult to obtain a significant improvement in Zr-based materials. The coating design can protect the cladding from oxidation. However, the main issue associated with the coating technology is the compatibility of the coating material with the zircaloy, including the matching of the thermal explosion coefficient, the diametrical compression, microstructure, and interdiffusion with Zr. Thus, alternative cladding materials have been proposed. Owing to the diversity of alternative materials, this review summarized the neutronic and thermophysical properties of FeCrAl- and SiC-based cladding materials.

The development of the ATF also allows the development and deployment of other fuels, including the advanced designs of the present UO_2 fuel (e.g., the FCM fuel design), the current UO_2 fuel doped with other materials to improve the thermal conductivity, and alternative fuels. The present review focused on BeO and Mo-doped UO_2 fuels, U_3Si_2 fuel, and UN fuel. In addition to the enhanced thermal conductivity, U_3Si_2 and UN have a higher U density than the current UO_2 fuel.

Because neutronic evaluation is fundamental for the application of enhanced ATF systems, we reviewed neutronic studies on different ATF systems. Regarding the coating technology, because the coating layer is significantly thinner than the cladding, the neutronic performance should be close to that of the current UO_2–Zr system, with the exception of the neutron economy. The additional coating material in the cladding leads to greater neutron absorption by materials other than U, and the cycle length is reduced if the same type of fuel is used. Nevertheless, this issue can be easily resolved by slightly increasing the ^{235}U enrichment.

In the case of using alternative fuels or alternative cladding materials, the neutronic performance differs from that of the current UO_2–Zr system, because of the changes in the neutron flux spectrum. The inherent safety level is also changed with the B coefficient and control rod worth, as well as the FTC, MTC, and VRC. Moreover, different power distributions lead to differences in the fuel temperature distribution and the subsequent thermomechanical performance of the fuel. Consequently, considerable modification of the reactor core design is needed to use the alternative fuel-cladding systems. This is why alternative fuels and cladding materials are difficult to deploy in the short term.

In summary, many types of potential accident-tolerant fuel-cladding systems were discussed in the present review. Although difficulties exist and further investigations should

be performed, it is expected that one or more of the discussed systems will be implemented in commercial reactors.

Acknowledgements Computational resources were provided by Sun Yat-sen University and the National Supercomputer Center in Guangzhou.

References

1. International Energy Agency, Electricity Statistics—2017. https://www.iea.org/statistics/electricity/. Accessed 19 Nov 2019
2. S.J. Zinkle, K.A. Terrani, J.C. Gehin et al., Accident tolerant fuels for LWRs: a perspective. J. Nucl. Mater. **448**, 374–379 (2014). https://doi.org/10.1016/j.jnucmat.2013.12.005
3. A.T. Nelson, Development of novel nuclear fuel materials for light water reactors. Trans. Am. Nucl. Soc. **118**, 1314–1317 (2018)
4. J.K. Fink, Thermophysical properties of uranium dioxide. J. Nucl. Mater. **279**, 1–18 (2000). https://doi.org/10.1016/S0022-3115(99)00273-1
5. P.G. Lucuta, H. Matzke, I.J. Hastings, A pragmatic approach to modelling thermal conductivity of irradiated UO_2 fuel: review and recommendations. J. Nucl. Mater. **232**, 166–180 (1996). https://doi.org/10.1016/S0022-3115(96)00404-7
6. J. Kruszelnicki, P. Moo, J. Rosales, et al., Property Analysis and Advanced Manufacturing Technique Development for Light Water Reactor Annular Composite Fuel (American Nuclear Society—ANS, La Grange Park, 2016), p. 160. https://www.osti.gov/biblio/22765197-property-analysis-advanced-manufacturing-technique-development-light-water-reactor-annular-composite-fuel. Accessed 31 Oct 2019
7. Nuclear Energy Agency, *State-of-the-art report on light water reactor accident-tolerant fuels* (OECD, Paris, 2018). https://doi.org/10.1787/9789264308343-en
8. A. Santamarina, D. Bernard, P. Blaise et al., *The JEFF-3.1.1 Nuclear Data Library* (OECD/NEA, Paris, 2009)
9. C. Vaglio-Gaudard, A. Santamarina, P. Blaise et al., Interpretation of PERLE experiment for the validation of iron nuclear data using monte carlo calculations. Nucl. Sci. Eng. **166**, 89–106 (2010). https://doi.org/10.13182/NSE09-91
10. S. Ravaux, *Qualification du Calcul de l'Échauffement Photonique dans les Réacteurs Nucléaires* (Université de Grenoble, Grenoble, 2013)
11. M. Diakaki, S. Chen, P. Tamagno, et al., Evaluation of n + ^{56}Fe Reaction Data (+Covariances) and Experimental Validation (IAEA, Vienna, 2018). https://www-nds.iaea.org/index-meeting-crp/CM-INDEN-III-2018/. Accessed 5 Nov 2019
12. S. Chen, D. Bernard, Attenuation of atomic displacement damage in the heavy reflector of the PERLE experiment and application to EPR. Nucl. Eng. Des. **353**, 110205 (2019). https://doi.org/10.1016/j.nucengdes.2019.110205
13. M. Diakaki, S. Chen, G. Noguere, et al., Evaluation of neutron induced reactions on ^{56}Fe with CONRAD. 2019 International Conference On Nuclear Data for Science and Technology (ND2019), May 19–24, 2019, in Beijing, China
14. S. Chen, C. Yuan, Neutronic analysis on potential accident tolerant fuel-cladding combination U_3Si_2–FeCrAl. Sci. Technol. Nucl. Install. **2017**, 3146985 (2017). https://doi.org/10.1155/2017/3146985
15. NEA, JEFF-3.3 Nuclear Data Library (2017). http://www.oecd-nea.org/dbdata/JEFF33
16. D.A. Brown, M.B. Chadwick, R. Capote et al., ENDF/B-VIII.0: the 8th major release of the nuclear reaction data library with CIELO-project cross sections, new standards and thermal scattering data. Nucl. Data Sheets **148**, 1–142 (2018). https://doi.org/10.1016/j.nds.2018.02.001
17. M. Murabayashi, S. Tanaka, Y. Takahashi, Thermal conductivity and heat capacity of zircaloy-2, -4 and unalloyed zirconium. J. Nucl. Sci. Technol. **12**, 661–662 (1975). https://doi.org/10.1080/18811248.1975.9733170
18. International Atomic Energy Agency, *Thermophysical Properties Database of Materials for Light Water Reactors and Heavy Water Reactors: Final Report of a Coordinated Research Project, 1999–2005* (International Atomic Energy Agency, Vienna, 2006)
19. J.J. Kearns, Terminal solubility and partitioning of hydrogen in the alpha phase of zirconium, zircaloy-2 and zircaloy-4. J. Nucl. Mater. **22**, 292–303 (1967). https://doi.org/10.1016/0022-3115(67)90047-5
20. B. Wang, C. Zhang, X. Ma et al., Key problems on the mechanical behavior of nuclear materials and structures of pressured water reactors. Sci. Sin. Phys. Mech. Astron. **49**, 114602 (2019). https://doi.org/10.1360/SSPMA-2019-0113
21. C. Zhang, P. Chen, J. Zhang et al., Evaluation of the structural integrity of the CPR1000 PWR containment under steam explosion accidents. Nucl. Eng. Des. **278**, 632–643 (2014). https://doi.org/10.1016/j.nucengdes.2014.08.019
22. K. Hauffe, Oxidation and corrosion of tin-coated zircaloy-4. J. Electrochem. Soc. **123**, 595 (1976). https://doi.org/10.1149/1.2132892
23. K. Sridharan, S.P. Harrington, A.K. Johnson, J.R. Licht, M.H. Anderson, T.R. Allen, Oxidation of plasma surface modified zirconium alloy in pressurized high temperature water. Mater. Des. **28**, 1177–1185 (2007). https://doi.org/10.1016/j.matdes.2006.01.019
24. K.A. Terrani, Accident tolerant fuel cladding development: promise, status, and challenges. J. Nucl. Mater. **501**, 13–30 (2018). https://doi.org/10.1016/j.jnucmat.2017.12.043
25. J. Bischoff, C. Delafoy, C. Vauglin et al., AREVA NP's enhanced accident-tolerant fuel developments: focus on Cr-coated M5 cladding. Nucl. Eng. Technol. **50**, 223–228 (2018). https://doi.org/10.1016/j.net.2017.12.004
26. J.-C. Brachet, M. Le Saux, M. Flem, S. Urvoy, E. Rouesne, T. Guilbert, C. Cobac, F. Lahogue, J. Rousselot, M. Tupin, P. Billaud, C. Hossepied, F. Schuster, F. Lomello, A. Billard, G. Velisa, E. Monsifrot, J. Bischoff, A. Ambard, On-going studies at CEA on chromium coated zirconium based nuclear fuel claddings for enhanced accident tolerant LWRs fuel. TopFuel 2015, September 13–19, 2015, in Zurich, Switzerland
27. J.-C. Brachet, C. Lorrette, A. Michaux, et al., CEA studies on advanced nuclear fuel claddings for enhanced accident tolerant LWRs fuel (LOCA and beyond LOCA conditions), in Avignon, France (2014). https://doi.org/10.13140/2.1.5105.6325
28. I. Idarraga-Trujillo, M.L. Flem, J.-C. Brachet, et al. Assessment at CEA of coated nuclear fuel cladding for LWRs with increasing margins in LOCA and beyond LOCA conditions, in *LWR Fuel Performance Meeting TopFuel 2013* (2013), p. 9
29. J.-H. Park, H.-G. Kim, J. Park et al., High temperature steam-oxidation behavior of arc ion plated Cr coatings for accident tolerant fuel claddings. Surf. Coat. Technol. **280**, 256–259 (2015). https://doi.org/10.1016/j.surfcoat.2015.09.022
30. H.-G. Kim, I.-H. Kim, Y.-I. Jung et al., Adhesion property and high-temperature oxidation behavior of Cr-coated zircaloy-4 cladding tube prepared by 3D laser coating. J. Nucl. Mater. **465**, 531–539 (2015). https://doi.org/10.1016/j.jnucmat.2015.06.030
31. H.-G. Kim, I.-H. Kim, Y.-I. Jung, et al., High-temperature oxidation behavior of Cr-coated zirconium alloy. In TopFuel

2013, September 15–19, 2013, in Charlotte, North Carolina, USA
32. X. He, Z. Tian, B. Shi et al., Effect of gas pressure and bias potential on oxidation resistance of Cr coatings. Ann. Nucl. Energy **132**, 243–248 (2019). https://doi.org/10.1016/j.anucene.2019.04.038
33. H. Yeom, B. Maier, G. Johnson et al., High temperature oxidation and microstructural evolution of cold spray chromium coatings on zircaloy-4 in steam environments. J. Nucl. Mater. **526**, 151737 (2019). https://doi.org/10.1016/j.jnucmat.2019.151737
34. L. Jiang, P. Xiu, Y. Yan et al., Effects of ion irradiation on chromium coatings of various thicknesses on a zirconium alloy. J. Nucl. Mater. **526**, 151740 (2019). https://doi.org/10.1016/j.jnucmat.2019.151740
35. W. Zhong, P.A. Mouche, B.J. Heuser, Response of Cr and Cr–Al coatings on zircaloy-2 to high temperature steam. J. Nucl. Mater. **498**, 137–148 (2018). https://doi.org/10.1016/j.jnucmat.2017.10.021
36. H.-G. Kim, I.-H. Kim, Y.-I. Jung, et al., Progress of surface modified Zr cladding development for ATF at KAERI. 2017 Water Reactor Fuel Performance Meeting, September 10–14, 2017, in Jeju, Korea
37. W. Zhong, P.A. Mouche, X. Han et al., Performance of iron–chromium–aluminum alloy surface coatings on zircaloy 2 under high-temperature steam and normal BWR operating conditions. J. Nucl. Mater. **470**, 327–338 (2016). https://doi.org/10.1016/j.jnucmat.2015.11.037
38. D.J. Park, H.G. Kim, Y.I. Jung et al., Behavior of an improved Zr fuel cladding with oxidation resistant coating under loss-of-coolant accident conditions. J. Nucl. Mater. **482**, 75–82 (2016). https://doi.org/10.1016/j.jnucmat.2016.10.021
39. K.A. Terrani, C.M. Parish, D. Shin et al., Protection of zirconium by alumina- and chromia-forming iron alloys under high-temperature steam exposure. J. Nucl. Mater. **438**, 64–71 (2013). https://doi.org/10.1016/j.jnucmat.2013.03.006
40. J.-W. Yeh, S.-K. Chen, S.-J. Lin et al., Nanostructured high-entropy alloys with multiple principal elements: novel alloy design concepts and outcomes. Adv. Eng. Mater. **6**, 299–303 (2004). https://doi.org/10.1002/adem.200300567
41. W. Zhang, R. Tang, Z.B. Yang et al., Preparation, structure, and properties of an AlCrMoNbZr high-entropy alloy coating for accident-tolerant fuel cladding. Surf. Coat. Technol. **347**, 13–19 (2018). https://doi.org/10.1016/j.surfcoat.2018.04.037
42. W. Zhang, R. Tang, Z.B. Yang et al., Preparation, structure, and properties of high-entropy alloy multilayer coatings for nuclear fuel cladding: a case study of AlCrMoNbZr/(AlCrMoNbZr)N. J. Nucl. Mater. **512**, 15–24 (2018). https://doi.org/10.1016/j.jnucmat.2018.10.001
43. U.D. Abdelrazek, S.W. Sharkawy, H.A. El-Sayed, Pyrolytic carbon coating of zircaloy-4 tubes at relatively low temperatures. J. Nucl. Mater. **249**, 159–164 (1997). https://doi.org/10.1016/S0022-3115(97)00214-6
44. C. Tang, M. Stueber, J. Hans et al., Protective coatings on zirconium-based alloys as accident-tolerant fuel (ATF) claddings. Corros. Rev. **35**, 141 (2017). https://doi.org/10.1515/corrrev-2017-0010
45. I. Kratochvílová, R. Škoda, J. Škarohlíd et al., Nanosized polycrystalline diamond cladding for surface protection of zirconium nuclear fuel tubes. J. Mater. Process. Technol. **214**, 2600–2605 (2014). https://doi.org/10.1016/j.jmatprotec.2014.05.009
46. P. Ashcheulov, R. Škoda, J. Škarohlíd et al., Thin polycrystalline diamond films protecting zirconium alloys surfaces: from technology to layer analysis and application in nuclear facilities. Appl. Surf. Sci. **359**, 621–628 (2015). https://doi.org/10.1016/j.apsusc.2015.10.117
47. H.-G. Kim, I.-H. Kim, J.-Y. Park et al., Application of coating technology on zirconium-based alloy to decrease high-temperature oxidation, in *Zirconium in the Nuclear Industry*, vol. 17, ed. by B. Comstock, P. Barberis (ASTM International, West Conshohocken, 2015), pp. 346–369. https://doi.org/10.1520/stp154320120161
48. H. Yeom, B. Maier, R. Mariani et al., Magnetron sputter deposition of zirconium-silicide coating for mitigating high temperature oxidation of zirconium-alloy. Surf. Coat. Technol. **316**, 30–38 (2017). https://doi.org/10.1016/j.surfcoat.2017.03.018
49. H. Yeom, C. Lockhart, R. Mariani et al., Evaluation of steam corrosion and water quenching behavior of zirconium-silicide coated LWR fuel claddings. J. Nucl. Mater. **499**, 256–267 (2018). https://doi.org/10.1016/j.jnucmat.2017.11.045
50. E. Alat, A.T. Motta, R.J. Comstock et al., Ceramic coating for corrosion (c3) resistance of nuclear fuel cladding. Surf. Coat. Technol. **281**, 133–143 (2015). https://doi.org/10.1016/j.surfcoat.2015.08.062
51. E. Alat, A.T. Motta, R.J. Comstock et al., Multilayer (TiN, TiAlN) ceramic coatings for nuclear fuel cladding. J. Nucl. Mater. **478**, 236–244 (2016). https://doi.org/10.1016/j.jnucmat.2016.05.021
52. X.-F. Ma, Y.-W. Wu, J. Tan et al., Evaluation of corrosion and oxidation behaviors of TiAlCrN coatings for nuclear fuel cladding. Surf. Coat. Technol. **358**, 521–530 (2019). https://doi.org/10.1016/j.surfcoat.2018.11.083
53. K. Daub, R. Van Nieuwenhove, H. Nordin, Investigation of the impact of coatings on corrosion and hydrogen uptake of Zircaloy-4. J. Nucl. Mater. **467**, 260–270 (2015). https://doi.org/10.1016/j.jnucmat.2015.09.041
54. C. Meng, L. Yang, Y. Wu, Study of the oxidation behavior of CrN coating on Zr alloy in air. J. Nucl. Mater. **515**, 354–369 (2019). https://doi.org/10.1016/j.jnucmat.2019.01.006
55. Y. Lee, J.I. Lee, H.C. No, Mechanical analysis of surface-coated zircaloy cladding. Nucl. Eng. Technol. **49**, 1031–1043 (2017). https://doi.org/10.1016/j.net.2017.03.012
56. W. Xiao, H. Deng, S. Zou et al., Effect of roughness of substrate and sputtering power on the properties of TiN coatings deposited by magnetron sputtering for ATF. J. Nucl. Mater. **509**, 542–549 (2018). https://doi.org/10.1016/j.jnucmat.2018.07.011
57. W. Xiao, H. Chen, X. Liu et al., Thermal shock resistance of TiN-, Cr-, and TiN/Cr-coated zirconium alloy. J. Nucl. Mater. **526**, 151777 (2019). https://doi.org/10.1016/j.jnucmat.2019.151777
58. K.K. Mandapaka, R.S. Cahyadi, S. Yalisove et al., Corrosion behavior of ceramic-coated ZIRLO^{TM} exposed to supercritical water. J. Nucl. Mater. **498**, 495–504 (2018). https://doi.org/10.1016/j.jnucmat.2017.10.040
59. M.W. Barsoum, The $M_{N+1}AX_N$ phases: a new class of solids: thermodynamically stable nanolaminates. Prog. Solid State Chem. **28**, 201–281 (2000). https://doi.org/10.1016/S0079-6786(00)00006-6
60. D.J. Tallman, E.N. Hoffman, E.N. Caspi et al., Effect of neutron irradiation on select MAX phases. Acta Mater. **85**, 132–143 (2015). https://doi.org/10.1016/j.actamat.2014.10.068
61. B.R. Maier, B.L. Garcia-Diaz, B. Hauch et al., Cold spray deposition of Ti_2AlC coatings for improved nuclear fuel cladding. J. Nucl. Mater. **466**, 712–717 (2015). https://doi.org/10.1016/j.jnucmat.2015.06.028
62. H. Yeom, B. Hauch, G. Cao et al., Laser surface annealing and characterization of Ti_2AlC plasma vapor deposition coating on zirconium-alloy substrate. Thin Solid Films **615**, 202–209 (2016). https://doi.org/10.1016/j.tsf.2016.07.024

63. D.A. Roberts, Magnetron sputtering and corrosion of Ti–Al–C and Cr–Al–C coatings for Zr-alloy nuclear fuel cladding, Master thesis, University of Tennessee, 2016
64. J. Wang, S. Liu, D. Ren et al., Microstructural evolution of epitaxial Ti_3AlC_2 film on sapphire under ion irradiation and nanoindentation-induced deformation. J. Nucl. Mater. **509**, 181–187 (2018). https://doi.org/10.1016/j.jnucmat.2018.06.045
65. D.J. Tallman, J. Yang, L. Pan et al., Reactivity of zircaloy-4 with Ti_3SiC_2 and Ti_2AlC in the 1100–1300 °C temperature range. J. Nucl. Mater. **460**, 122–129 (2015). https://doi.org/10.1016/j.jnucmat.2015.02.006
66. M. Ougier, A. Michau, F. Lomello et al., High-temperature oxidation behavior of HiPIMS as-deposited Cr–Al–C and annealed Cr_2AlC coatings on Zr-based alloy. J. Nucl. Mater. **528**, 151855 (2020). https://doi.org/10.1016/j.jnucmat.2019.151855
67. W. Bao, J. Xue, J.-X. Liu et al., Coating SiC on zircaloy-4 by magnetron sputtering at room temperature. J. Alloys Compd. **730**, 81–87 (2018). https://doi.org/10.1016/j.jallcom.2017.09.281
68. H.-G. Kim, J.-H. Yang, W.-J. Kim et al., Development status of accident-tolerant fuel for light water reactors in Korea. Nucl. Eng. Technol. **48**, 1–15 (2016). https://doi.org/10.1016/j.net.2015.11.011
69. H.-G. Kim, I.-H. Kim, Y.-I. Jung, D.-J. Park, J.-Y. Park, Y.-H. Koo, Microstructure and mechanical strength of surface ODS treated zircaloy-4 sheet using laser beam scanning. Nucl. Eng. Technol. **46**, 521–528 (2014). https://doi.org/10.5516/NET.07.2014.027
70. H.-G. Kim, I.-H. Kim, Y.-I. Jung, et al., Development of surface modified Zr cladding by coating technology for ATF. TopFuel 2016, September 11–15, 2016, in Boise, ID
71. J.R. Conrad, J.L. Radtke, R.A. Dodd et al., Plasma source ion-implantation technique for surface modification of materials. J. Appl. Phys. **62**, 4591–4596 (1987). https://doi.org/10.1063/1.339055
72. D.Q. Peng, X.D. Bai, F. Pan et al., Influence of aluminum ions implanted on oxidation behavior of ZIRLO alloy at 500 °C. Vacuum **80**, 530–536 (2006). https://doi.org/10.1016/j.vacuum.2005.08.026
73. C. Yuan, X. Wang, S. Chen, A simple formula for local burnup and isotope distributions based on approximately constant relative reaction rate. Sci. Technol. Nucl. Install. **2016**, 6980547 (2016). https://doi.org/10.1155/2016/6980547
74. J.M. Harp, P.A. Lessing, R.E. Hoggan, Uranium silicide pellet fabrication by powder metallurgy for accident tolerant fuel evaluation and irradiation. J. Nucl. Mater. **466**, 728–738 (2015). https://doi.org/10.1016/j.jnucmat.2015.06.027
75. R. Mariani, V.S. Blackwood, Z.S. Jones, et al., New fuel alloys seeking optimal solidus and phase behavior for high burnup and TRU burning. International Conference on Fast Reactors and Related Fuel Cyles: Safe Technologies and Sustainable Scenarios (FR13), March 2013, in Paris, France
76. Y.S. Kim, G.L. Hofman, A.M. Yacout et al., U-Mo alloy fuel for TRU-burning advanced fast reactors. J. Nucl. Mater. **441**, 520–524 (2013). https://doi.org/10.1016/j.jnucmat.2013.01.324
77. E.J. Lahoda, F.A. Boylan, *Development of LWR Fuels with Enhanced Accident Tolerance* (Westinghouse Electric Company, LLC, Cranberry Woods, 2015). https://doi.org/10.2172/1233713
78. Y.S. Touloukian, T. Makita, *Thermophysical Properties of Matter—The TPRC Data Series* (Thermophysical Properties Research Center, Wilmington, 1970)
79. W. Zhou, W. Zhou, Thermophysical and mechanical analyses of UO_2–36.4 vol% BeO fuel pellets with zircaloy, SiC, and FeCrAl claddings. Metals **8**, 65 (2018). https://doi.org/10.3390/met8010065
80. J.H. Harding, D.G. Martin, A recommendation for the thermal conductivity of UO_2. J. Nucl. Mater. **166**, 223–226 (1989). https://doi.org/10.1016/0022-3115(89)90218-3
81. P.G. Lucuta, R.A. Verrall, H. Matzke et al., Microstructural features of SIMFUEL—simulated high-burnup UO_2-based nuclear fuel. J. Nucl. Mater. **178**, 48–60 (1991). https://doi.org/10.1016/0022-3115(91)90455-g
82. S. Ishimoto, M. Hirai, K. Ito et al., Thermal conductivity of UO_2–BeO pellet. J. Nucl. Sci. Technol. **33**, 134–140 (1996). https://doi.org/10.3327/jnst.33.134
83. D.S. Li, H. Garmestani, J. Schwartz, Modeling thermal conductivity in UO_2 with BeO additions as a function of microstructure. J. Nucl. Mater. **392**, 22–27 (2009). https://doi.org/10.1016/j.jnucmat.2009.03.048
84. D.E. Johnson, R.G. Mills, *Irradiation Behavior of BeO–UO_2 Fuel as a Function of Fuel-Particle Size* (General Atomic Division of United States Atomic Energy Commission, San Diego, 1963)
85. D. Chandramouli, S.T. Revankar, Development of thermal models and analysis of UO_2–BeO fuel during a loss of coolant accident. Int. J. Nucl. Energy **2014**, 1–9 (2014). https://doi.org/10.1155/2014/751070
86. J.R. Smith, *Enhanced Thermal Conductivity UO_2–BeO Nuclear Fuel: Neutronic Performance Studies and Economic Analyses* (Texas A&M University, College Station, 2012)
87. K. McCoy, C. Mays, Enhanced thermal conductivity oxide nuclear fuels by co-sintering with BeO: II. Fuel performance and neutronics. J. Nucl. Mater. **375**, 157–167 (2008). https://doi.org/10.1016/j.jnucmat.2007.10.014
88. S.K. Kim, W.I. Ko, H.D. Kim et al., Cost–benefit analysis of BeO–UO_2 nuclear fuel. Prog. Nucl. Energy **52**, 813–821 (2010). https://doi.org/10.1016/j.pnucene.2010.07.008
89. D.E. Burkes, A.M. Casella, A.J. Casella et al., Thermal properties of U–Mo alloys irradiated to moderate burnup and power. J. Nucl. Mater. **464**, 331–341 (2015). https://doi.org/10.1016/j.jnucmat.2015.04.040
90. A.T. Nelson, E.S. Sooby, Y.-J. Kim et al., High temperature oxidation of molybdenum in water vapor environments. J. Nucl. Mater. **448**, 441–447 (2014). https://doi.org/10.1016/j.jnucmat.2013.10.043
91. A. Nelson, J. White, D. Byler et al., Overview of properties and performance of uranium-silicide compounds for light water reactor applications. Trans. Am. Nucl. Soc. **110**, 987–989 (2014)
92. G.L. Hofman, Crystal structure stability and fission gas swelling in intermetallic uranium compounds. J. Nucl. Mater. **140**, 256–263 (1986). https://doi.org/10.1016/0022-3115(86)90208-4
93. N.R. Brown, M. Todosow, A. Cuadra, Screening of advanced cladding materials and UN–U_3Si_5 fuel. J. Nucl. Mater. **462**, 26–42 (2015). https://doi.org/10.1016/j.jnucmat.2015.03.016
94. M.R. Finlay, G.L. Hofman, J.L. Snelgrove, Irradiation behaviour of uranium silicide compounds. J. Nucl. Mater. **325**, 118–128 (2004). https://doi.org/10.1016/j.jnucmat.2003.11.009
95. K. Metzger, T. Knight, R. Williamson, Model of U_3Si_2 fuel system using BISON fuel code, in *Proceedings of the ICAPP 2014, Charlotte, USA* (2014)
96. H. Shimizu, *The Properties and Irradiation Behavior of U_3Si_2* (Atomics International, Canoga Park, 1965). https://doi.org/10.2172/4639974
97. S.B. Ross, M.S. El-Genk, R.B. Matthews, Thermal conductivity correlation for uranium nitride fuel between 10 and 1923 K. J. Nucl. Mater. **151**, 318–326 (1988). https://doi.org/10.1016/0022-3115(88)90026-8
98. S.L. Hayes, J.K. Thomas, K.L. Peddicord, Material property correlations for uranium mononitride: I. Physical properties.

J. Nucl. Mater. **171**, 262–270 (1990). https://doi.org/10.1016/0022-3115(90)90374-v
99. K.Y. Spencer, L. Sudderth, R.A. Brito et al., Sensitivity study for accident tolerant fuels: property comparisons and behavior simulations in a simplified PWR to enable ATF development and design. Nucl. Eng. Des. **309**, 197–212 (2016). https://doi.org/10.1016/j.nucengdes.2016.09.009
100. L.M. Ferris, Reactions of uranium mononitride, thorium monocarbide and uranium monocarbide with nitric acid and other aqueous reagents. J. Inorg. Nucl. Chem. **30**, 2661–2669 (1968)
101. D.A. Lopes, S. Uygur, K. Johnson, Degradation of UN and UN–U_3Si_2 pellets in steam environment. J. Nucl. Sci. Technol. **54**, 405–413 (2017). https://doi.org/10.1080/00223131.2016.1274689
102. J.H. Yang, D.-J. Kim, K.S. Kim et al., UO_2–UN composites with enhanced uranium density and thermal conductivity. J. Nucl. Mater. **465**, 509–515 (2015). https://doi.org/10.1016/j.jnucmat.2015.06.039
103. K.D. Johnson, A.M. Raftery, D.A. Lopes et al., Fabrication and microstructural analysis of UN–U_3Si_2 composites for accident tolerant fuel applications. J. Nucl. Mater. **477**, 18–23 (2016). https://doi.org/10.1016/j.jnucmat.2016.05.004
104. J.J. Powers, W.J. Lee, F. Venneri et al., *Fully Ceramic Microencapsulated (FCM) Replacement Fuel for LWRs* (ORNL, Oak Ridge, 2013). https://doi.org/10.2172/1087039
105. N.R. Brown, H. Ludewig, A. Aronson et al., Neutronic evaluation of a PWR with fully ceramic microencapsulated fuel. Part I: lattice benchmarking, cycle length, and reactivity coefficients. Ann. Nucl. Energy **62**, 538–547 (2013). https://doi.org/10.1016/j.anucene.2013.05.025
106. N.M. George, I. Maldonado, K. Terrani et al., Neutronics studies of uranium-bearing fully ceramic microencapsulated fuel for pressurized water reactors. Nucl. Technol. **188**, 238–251 (2014). https://doi.org/10.13182/NT14-3
107. C.F. Cheng, Corrosion aspects of iron, austenitic stainless steel and inconel in high temperature water. Corrosion **20**, 341t–349t (1964). https://doi.org/10.5006/0010-9312-20.11.341t
108. F. Garzarolli, R. von Jan, H. Stehle, The main causes of fuel element failure in water-cooled power reactors. At. Energy Rev. **17**, 31–128 (1979)
109. A. Strasser, J. Santucci, K. Lindquist et al., *Evaluation of Stainless Steel Cladding for Use in Current Design LWRs* (Stoller (SM) Corp, New York, 1982)
110. K.A. Terrani, S.J. Zinkle, L.L. Snead, Advanced oxidation-resistant iron-based alloys for LWR fuel cladding. J. Nucl. Mater. **448**, 420–435 (2014). https://doi.org/10.1016/j.jnucmat.2013.06.041
111. E.A. Gulbransen, K.F. Andrew, Oxidation studies on the ion-chromium-aluminum heater alloys. J. Electrochem. Soc. **106**, 294–302 (1959). https://doi.org/10.1149/1.2427333
112. K.A. Unocic, Y. Yamamoto, B.A. Pint, Effect of Al and Cr content on air and steam oxidation of FeCrAl alloys and commercial APMT alloy. Oxid. Met. **87**, 431–441 (2017). https://doi.org/10.1007/s11085-017-9745-1
113. R.B. Rebak, N.R. Brown, K.A. Terrani, Assessment of advanced steels as accident tolerant fuel cladding for commercial LWRs. 17th International Conference on Environmental Degradation of Materials in Nuclear Power Systems – Water Reactors, 9–12 August 2015, Ottawa, Ontario, Canada, p. 227
114. L.J. Ott, K.R. Robb, D. Wang, Preliminary assessment of accident-tolerant fuels on LWR performance during normal operation and under DB and BDB accident conditions. J. Nucl. Mater. **448**, 520–533 (2014). https://doi.org/10.1016/j.jnucmat.2013.09.052
115. S. Chen, D. Bernard, On the calculation of atomic displacements using damage energy. Results Phys. **16**, 102835 (2020). https://doi.org/10.1016/j.rinp.2019.102835
116. Hatch Unit Restarts with Accident-Tolerant Fuel. http://www.world-nuclear-news.org/UF-Hatch-unit-restarts-with-accident-tolerant-fuel-0703184.html. Accessed 13 Apr 2018
117. S. Chen, D. Bernard, Relativistic effect on two-body reaction inducing atomic displacement. J. Nucl. Mater. **522**, 236–245 (2019). https://doi.org/10.1016/j.jnucmat.2019.05.020
118. R.E. MacFarlane, D.W. Muir, F.M. Mann, Radiation damage calculations with NJOY. J. Nucl. Mater. **123**, 1041–1046 (1984). https://doi.org/10.1016/0022-3115(84)90216-2
119. S. Chen, D. Bernard, P. Tamagno et al., Calculation and verification of neutron irradiation damage with differential cross sections. Nucl. Instrum. Methods Phys. Res. Sect. B Beam Interact. Mater. At. **456**, 120–132 (2019). https://doi.org/10.1016/j.nimb.2019.07.011
120. S. Chen, D. Bernard, L. Buiron, Study on the self-shielding and temperature influences on the neutron irradiation damage calculations in reactors. Nucl. Eng. Des. **346**, 85–96 (2019). https://doi.org/10.1016/j.nucengdes.2019.03.006
121. S. Chen, D. Bernard, C. De Saint Jean, Calculation and analysis of gamma-induced irradiation damage cross section. Nucl. Instrum. Methods Phys. Res. Sect. B Beam Interact. Mater. At. **447**, 8–21 (2019). https://doi.org/10.1016/j.nimb.2019.03.035
122. K.G. Field, X. Hu, K.C. Littrell et al., Radiation tolerance of neutron-irradiated model Fe–Cr–Al alloys. J. Nucl. Mater. **465**, 746–755 (2015). https://doi.org/10.1016/j.jnucmat.2015.06.023
123. S.A. Briggs, P.D. Edmondson, K.C. Littrell et al., A combined APT and SANS investigation of α' phase precipitation in neutron-irradiated model FeCrAl alloys. Acta Mater. **129**, 217–228 (2017). https://doi.org/10.1016/j.actamat.2017.02.077
124. S. Dryepondt, K.A. Unocic, D.T. Hoelzer et al., Development of low-Cr ODS FeCrAl alloys for accident-tolerant fuel cladding. J. Nucl. Mater. **501**, 59–71 (2018). https://doi.org/10.1016/j.jnucmat.2017.12.035
125. J.W. McMurray, R. Hu, S.V. Ushakov et al., Solid-liquid phase equilibria of Fe–Cr–Al alloys and spinels. J. Nucl. Mater. **492**, 128–133 (2017). https://doi.org/10.1016/j.jnucmat.2017.05.016
126. B.A. Pint, K.A. Terrani, Y. Yamamoto et al., Material selection for accident tolerant fuel cladding. Metall. Mater. Trans. E **2**, 190–196 (2015). https://doi.org/10.1007/s40553-015-0056-7
127. B. Qiu, J. Wang, Y. Deng et al., A review on thermohydraulic and mechanical-physical properties of SiC, FeCrAl and Ti_3SiC_2 for ATF cladding. Nucl. Eng. Technol. **52**, 1–13 (2020). https://doi.org/10.1016/j.net.2019.07.030
128. Kanthal®, Kanthal® APMT. https://www.kanthal.com/en/products/material-datasheets/tube/kanthal-apmt/. Accessed 5 Nov 2019
129. R.A. Holt, Mechanisms of irradiation growth of alpha-zirconium alloys. J. Nucl. Mater. **159**, 310–338 (1988). https://doi.org/10.1016/0022-3115(88)90099-2
130. S.J. Zinkle, P.J. Maziasz, R.E. Stoller, Dose dependence of the microstructural evolution in neutron-irradiated austenitic stainless steel. J. Nucl. Mater. **206**, 266–286 (1993). https://doi.org/10.1016/0022-3115(93)90128-L
131. S.I. Porollo, YuV Konobeev, A.M. Dvoriashin et al., Void swelling at low displacement rates in annealed 12X18HgT stainless steel at 4–56 dpa and 280–332 °C. J. Nucl. Mater. **307–311**, 339–342 (2002). https://doi.org/10.1016/S0022-3115(02)01551-9
132. X. Wu, T. Kozlowski, J.D. Hales, Neutronics and fuel performance evaluation of accident tolerant FeCrAl cladding under normal operation conditions. Ann. Nucl. Energy **85**, 763–775 (2015). https://doi.org/10.1016/j.anucene.2015.06.032

133. K.A. Terrani, B.A. Pint, Y.-J. Kim et al., Uniform corrosion of FeCrAl alloys in LWR coolant environments. J. Nucl. Mater. **479**, 36–47 (2016). https://doi.org/10.1016/j.jnucmat.2016.06.047
134. D. Levchuk, H. Bolt, M. Döbeli et al., Al–Cr–O thin films as an efficient hydrogen barrier. Surf. Coat. Technol. **202**, 5043–5047 (2008). https://doi.org/10.1016/j.surfcoat.2008.05.012
135. R.A. Causey, R.A. Karnesky, C. San Marchi, 4.16—tritium barriers and tritium diffusion in fusion reactors, in *Comprehensive Nuclear Materials*, ed. by R.J.M. Konings (Elsevier, Oxford, 2012), pp. 511–549. https://doi.org/10.1016/b978-0-08-056033-5.00116-6
136. J. Liu, X. Zhang, D. Yun, A complete review and a prospect on the candidate materials for accident-tolerant fuel claddings. Mater. Rep. **32**, 1757–1778 (2018). https://doi.org/10.11896/j.issn.1005-023X.2018.11.001
137. Y. Katoh, L.L. Snead, C.H. Henager et al., Current status and critical issues for development of SiC composites for fusion applications. J. Nucl. Mater. **367–370**, 659–671 (2007). https://doi.org/10.1016/j.jnucmat.2007.03.032
138. Y. Katoh, K. Ozawa, C. Shih et al., Continuous SiC fiber, CVI SiC matrix composites for nuclear applications: properties and irradiation effects. J. Nucl. Mater. **448**, 448–476 (2014). https://doi.org/10.1016/j.jnucmat.2013.06.040
139. T. Koyanagi, K. Ozawa, T. Hinoki et al., Effects of neutron irradiation on mechanical properties of silicon carbide composites fabricated by nano-infiltration and transient eutectic-phase process. J. Nucl. Mater. **448**, 478–486 (2014). https://doi.org/10.1016/j.jnucmat.2013.10.005
140. C.M. Petrie, T. Koyanagi, J.L. McDuffee et al., Experimental design and analysis for irradiation of SiC/SiC composite tubes under a prototypic high heat flux. J. Nucl. Mater. **491**, 94–104 (2017). https://doi.org/10.1016/j.jnucmat.2017.04.058
141. W.-J. Kim, D. Kim, J.Y. Park, Fabrication and material issues for the application of sic composites to LWR fuel cladding. Nucl. Eng. Technol. **45**, 565–572 (2013). https://doi.org/10.5516/NET.07.2012.084
142. Y. Katoh, K.A. Terrani, *Systematic Technology Evaluation Program for SiC/SiC Composite-Based Accident-Tolerant LWR Fuel Cladding and Core Structures: Revision 2015* (Oak Ridge National Lab (ORNL), Oak Ridge, 2015). https://doi.org/10.2172/1215606
143. Y. Lee, M.S. Kazimi, A structural model for multi-layered ceramic cylinders and its application to silicon carbide cladding of light water reactor fuel. J. Nucl. Mater. **458**, 87–105 (2015). https://doi.org/10.1016/j.jnucmat.2014.12.013
144. Y. Lee, H.C. No, J.I. Lee, Design optimization of multi-layer silicon carbide cladding for light water reactors. Nucl. Eng. Des. **311**, 213–223 (2017). https://doi.org/10.1016/j.nucengdes.2016.11.016
145. B.-S. Li, Pellet Cladding Mechanical Interactions of Ceramic Claddings Fuels Under Light Water Reactor Conditions (University of South Carolina, Columbia, 2013). https://scholarcommons.sc.edu/etd/2366
146. J.P. Mazzoccoli, J. Choi, P. Xu, Progress on the Westinghouse Accident Tolerant Fuel Programme, IAEA. http://inis.iaea.org/Search/search.aspx?orig_q=RN:47080135. Accessed 7 Nov 2019
147. J.D. Stempien, D.M. Carpenter, G. Kohse et al., Characteristics of composite silicon carbide fuel cladding after irradiation under simulated PWR conditions. Nucl. Technol. **183**, 13–29 (2013). https://doi.org/10.13182/NT12-86
148. L.L. Snead, T. Nozawa, Y. Katoh et al., Handbook of SiC properties for fuel performance modeling. J. Nucl. Mater. **371**, 329–377 (2007). https://doi.org/10.1016/j.jnucmat.2007.05.016
149. R.J. Price, Properties of silicon carbide for nuclear fuel particle coatings. Nucl. Technol. **35**, 320–336 (1977). https://doi.org/10.13182/NT77-A31892
150. X. Dong, Y.C. Shin, Predictions of thermal conductivity and degradation of irradiated SiC/SiC composites by materials-genome-based multiscale modeling. J. Nucl. Mater. **512**, 268–275 (2018). https://doi.org/10.1016/j.jnucmat.2018.10.021
151. K.A. Terrani, B.A. Pint, C.M. Parish et al., Silicon carbide oxidation in steam up to 2 MPa. J. Am. Ceram. Soc. **97**, 2331–2352 (2014). https://doi.org/10.1111/jace.13094
152. J. Braun, C. Guéneau, T. Alpettaz et al., Chemical compatibility between UO_2 fuel and SiC cladding for LWRs. Application to ATF (accident-tolerant fuels). J. Nucl. Mater. **487**, 380–395 (2017). https://doi.org/10.1016/j.jnucmat.2017.02.031
153. I. Younker, M. Fratoni, Neutronic evaluation of coating and cladding materials for accident tolerant fuels. Prog. Nucl. Energy **88**, 10–18 (2016). https://doi.org/10.1016/j.pnucene.2015.11.006
154. S. Chen, C. Yuan, Neutronic study of UO_2–BeO Fuel with various claddings. Nucl. Mater. Energy **22**, 100728 (2020). https://doi.org/10.1016/j.nme.2020.100728
155. Q. Zhang, X. Wang, Y. Zhang et al., Neutronic analysis for potential accident tolerant fuel UO_2–BeO in the light water reactor. Ann. Nucl. Energy **127**, 278–292 (2019). https://doi.org/10.1016/j.anucene.2018.12.014
156. N.R. Brown, A. Aronson, M. Todosow et al., Neutronic performance of uranium nitride composite fuels in a PWR. Nucl. Eng. Des. **275**, 393–407 (2014). https://doi.org/10.1016/j.nucengdes.2014.04.040
157. N.M. George, K. Terrani, J. Powers et al., Neutronic analysis of candidate accident-tolerant cladding concepts in pressurized water reactors. Ann. Nucl. Energy **75**, 703–712 (2015). https://doi.org/10.1016/j.anucene.2014.09.005
158. N.R. Brown, A.J. Wysocki, K.A. Terrani et al., The potential impact of enhanced accident tolerant cladding materials on reactivity initiated accidents in light water reactors. Ann. Nucl. Energy **99**, 353–365 (2017). https://doi.org/10.1016/j.anucene.2016.09.033
159. D. Salazar, F. Franceschini, P. Ferroni, et al., I^2S-LWR fuel management option for an 18-month cycle length. Advances in Nuclear Fuel Management (ANFM '15), March 29, 2015, Hilton Head Island, SC, USA
160. S. Chen, C. Yuan, Minor actinides transmutation in candidate accident tolerant fuel-claddings U_3Si_2–FeCrAl and U_3Si_2–SiC. Ann. Nucl. Energy **127**, 204–214 (2019). https://doi.org/10.1016/j.anucene.2018.12.003
161. S. Chen, C. Yuan, D. Guo, Radial distributions of power and isotopic concentrations in candidate accident tolerant fuel U_3Si_2 and UO_2/U_3Si_2 fuel pins with FeCrAl cladding. Ann. Nucl. Energy **124**, 460–471 (2019). https://doi.org/10.1016/j.anucene.2018.10.025
162. R. Liu, W. Zhou, J. Cai, Multiphysics modeling of accident tolerant fuel-cladding U_3Si_2–FeCrAl performance in a light water reactor. Nucl. Eng. Des. **330**, 106–116 (2018). https://doi.org/10.1016/j.nucengdes.2018.01.041
163. S. Chen, Y. Ge, Y. Zhong et al., Radial distributions of power and fuel temperature in annular U_3Si_2 fuel with FeCrAl cladding. Ann. Nucl. Energy **135**, 106943 (2020). https://doi.org/10.1016/j.anucene.2019.106943